

# 1 Structural Properties

## 1.1 IONICITY

Details of ionicity  $f_i$  are given in Adachi [1]. Any given definition of ionicity is likely to be imperfect. We present in Table 1.1  $f_i$  values for a number of group-IV, III-V and II-VI semiconductors, including Be-based semiconductors and CdO. We have Phillips ionicity of  $f_i = 0$  for all group-IV elemental semiconductors (diamond, Si, Ge and  $\alpha$ -Sn) and  $f_i > 0.9$  for some alkali halides (NaCl, KCl, etc.).

Figure 1.1(a) plots  $f_i$  versus  $x$  for  $C_xSi_{1-x}$ . Note that  $f_i = 0.177$  for silicon carbide (SiC). This means that the bond character of SiC resembles that of III-V or II-VI semiconductors rather than of Si or diamond, so that its crystal structure must be zinc-blende, hexagonal or rhombohedral. Similarly, an ordered alloy of  $Si_xGe_{1-x}$  may have a nonzero  $f_i$  value near the ordered-phase composition  $x \sim 0.5$ . In fully disordered alloys ( $C_xSi_{1-x}$ ,  $Si_xGe_{1-x}$ , etc.), we should have  $f_i = 0$  over the whole alloy range  $0 \leq x \leq 1.0$ .

The plots of  $f_i$  versus  $x$  or  $y$  for  $Al_xGa_{1-x}As$ ,  $Ga_xIn_{1-x}P_yAs_{1-y}/InP$  and  $Mg_xZn_{1-x}S_ySe_{1-y}/GaAs$  are shown in Figure 1.1(b). These values are obtained from the linear interpolation of Equations (A.4) and (A.6) between the endpoint data in Table 1.1. The resulting  $f_i$  versus  $x$  ( $y$ ) plots can be expressed in the usual power form as

$$f_i(x) = 0.310 - 0.036x \quad (1.1a)$$

for  $Al_xGa_{1-x}As$ ,

$$f_i(y) = 0.335 + 0.065y + 0.021y^2 \quad (1.1b)$$

for  $Ga_xIn_{1-x}P_yAs_{1-y}/InP$  and

$$f_i(x) = 0.630 + 0.154x + 0.003x^2 \quad (1.1c)$$

for  $Mg_xZn_{1-x}S_ySe_{1-y}/GaAs$ . The values of  $f_i$  for fully disordered alloys should be safely estimated from the linear interpolation scheme.

## 1.2 ELEMENTAL ISOTOPIC ABUNDANCE AND MOLECULAR WEIGHT

In Tables 1.2 and 1.3 of Adachi [1], the elements which form at least one tetrahedrally coordinated  $A^N B^{8-N}$  semiconductor, together with their natural isotopic abundance in percent and atomic weight are listed. Let us add an element of beryllium: natural abundance of  ${}^9Be = 100\%$ ; atomic weight = 9.012182(3).

**Table 1.1** Phillips’s ionicity  $f_i$  for a number of group-IV, III–V and II–VI semiconductors

IV	$f_i$	III–V	$f_i$	II–VI	$f_i$
Diamond	0	BN	0.221	BeO	0.602
Si	0	BP	0.032	BeS	0.286
Ge	0	BAs	0.044	BeSe	0.261
Sn	0	AlN	0.449	BeTe	0.169
SiC	0.177	AlP	0.307	MgO	0.841
		AlAs	0.274	MgS	0.786
		AlSb	0.250	MgSe	0.790
		GaN	0.500	MgTe	0.554
		GaP	0.327	ZnO	0.616
		GaAs	0.310	ZnS	0.623
		GaSb	0.261	ZnSe	0.630
		InN	0.578	ZnTe	0.609
		InP	0.421	CdO	0.785
		InAs	0.357	CdS	0.685
		InSb	0.321	CdSe	0.699
				CdTe	0.717
				HgS	0.790
				HgSe	0.680
				HgTe	0.650

The molecular weight  $M$  for an  $A^N B^{8-N}$  compound semiconductor ( $N \neq 4$ ) can be simply given by the sum of the atomic weights of atoms A and B. For an elemental semiconductor ( $N = 4$ ), it is given by the atomic weight of the element atom  $A = B$ . The molecular weight  $M$  of any alloy semiconductors can be obtained from the linear interpolation scheme.

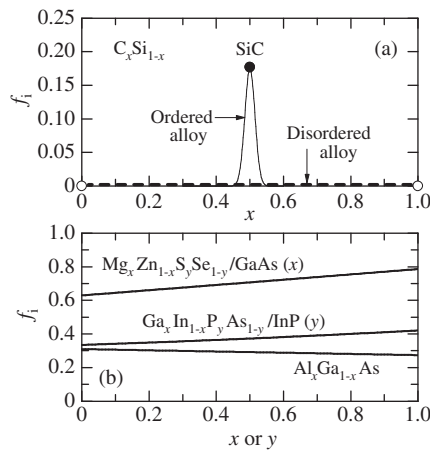


**Figure 1.1** Phillips ionicity  $f_i$  versus  $x$  or  $y$  for (a)  $C_xSi_{1-x}$  and (b)  $Al_xGa_{1-x}As$ ,  $Ga_xIn_{1-x}P_yAs_{1-y}/InP$  and  $Mg_xZn_{1-x}S_ySe_{1-y}/GaAs$ . The open and solid circles in (a) show the endpoint and SiC ( $x = 0.5$ ) values, respectively. The solid lines in (b) are calculated from Equation (1.1)

## 1.3 CRYSTAL STRUCTURE

### 1.3.1 Random Alloy

Table 1.2 summarizes the crystal classes for easily obtained or normally grown: (a) group-IV elemental semiconductors, (b) III–V and (c) II–VI binary semiconductors. In Table 1.2(a), the crystal classes for an easily grown compound semiconductor SiC are also included.

**Table 1.2** Summary of crystal structure for: (a) group-IV, (b) III–V and (c) II–VI semiconductors. d = diamond; zb = zinc-blende; w = wurtzite ( $C_{6v}$ ); h = hexagonal ( $C_{6v}$  or  $D_{6h}$ ); rh = rhombohedral; t = tetragonal; rs = rocksalt; or = orthorhombic. Note that  $\beta$ -Sn (t) is a metal

(a)				
IV	C	Si	Ge	Sn
C	d	zb, w, h, rh		
Si	zb, w, h, rh	d		
Ge			d	
Sn				d, t
(b)				
III/V	N	P	As	Sb
B	zb, h	zb	zb	
Al	w	zb	zb	zb
Ga	w	zb	zb	zb
In	w	zb	zb	zb
(c)				
II/VI	O	S	Se	Te
Be	w	zb	zb	zb
Mg	rs	rs	zb	w
Zn	w	zb, w	zb	zb
Cd	rs	w	w	zb
Hg	rh, or	zb, rh	zb	zb

### 1.3.2 Spontaneous Ordering

#### (a) Group-IV semiconductor alloy

The phenomenon of spontaneous ordering in semiconductor alloys is observed to occur spontaneously during epitaxial growth of certain semiconductor alloys and results in a modification of their structural, electronic and optical properties [2]. Substantial effort has been focused on learning how to control this phenomenon so that it may be used for tailoring desirable material properties. We summarize in Table 1.3 the spontaneous ordering phases observed in some group-IV, III–V and II–VI semiconductor alloys.

**Table 1.3** Types of spontaneous ordering phases observed in some group-IV, III-V and II-VI semiconductor alloys

System	Ordering type	Material	Epitaxial growth
IV	RS1 (CuPt)	SiGe	MBE <sup>a</sup>
	RS2 (CuPt)	SiGe	MBE <sup>a</sup>
	RS3 (CuPt)	SiGe	MBE <sup>a</sup>
III-V	CuPt-B	AlInP	MBE, <sup>b</sup> MOCVD <sup>c</sup>
		GaInP	Cl-VPE, <sup>d</sup> HT-VPE, <sup>e</sup> MBE, <sup>f</sup> MOCVD <sup>g</sup>
		AlInAs	MEB, <sup>h</sup> MOCVD <sup>i</sup>
		GaInAs	Cl-VPE, <sup>j</sup> MOCVD <sup>k</sup>
		GaInSb	MOCVD <sup>l</sup>
		GaPAs	MOCVD <sup>m</sup>
		GaPSb	MOCVD <sup>n</sup>
		GaAsSb	MBE <sup>o</sup>
		InPAs	MOCVD <sup>p</sup>
		InPSb	MOCVD <sup>q</sup>
		InAsSb	MOCVD, <sup>r</sup> MBE <sup>s</sup>
		GaInPAs	Cl-VPE, <sup>j</sup> MOCVD <sup>t</sup>
		AlGaInP	MOCVD <sup>c</sup>
	CuPt-A	AlInP	MBE <sup>b</sup>
		AlInAs	MBE <sup>u</sup>
	CuAu-I	AlGaAs	MOCVD <sup>v</sup>
		GaInAs	MBE <sup>w</sup>
GaAsSb		MBE, <sup>x</sup> MOCVD <sup>y</sup>	
TP-A	AlInAs	MBE <sup>z</sup>	
	GaInAs	MBE <sup>aa</sup>	
II-VI	CuPt-B	ZnCdTe	MOCVD <sup>ab</sup>
		CdHgTe	LPE <sup>ac</sup>
		ZnSeTe	MOCVD <sup>ad</sup>
	CuAu-I	ZnCdTe	MBE <sup>ae</sup>
		ZnSeTe	MBE <sup>af</sup>
	Cu <sub>3</sub> Au	ZnCdTe	MBE <sup>ag</sup>

<sup>a</sup>See, W. Jäger, in *Properties of Strained and Relaxed Silicon Germanium*, EMIS Datareviews Series No. 12 (edited by E. Kasper), INSPEC, London, 1995, p. 53

<sup>b</sup>A. Gomyo *et al.*, *Jpn. J. Appl. Phys.* **34**, L469 (1995)

<sup>c</sup>T. Suzuki *et al.*, *Jpn. J. Appl. Phys.* **27**, 2098 (1988)

<sup>d</sup>O. Ueta *et al.*, *J. Appl. Phys.* **68**, 4268 (1990)

<sup>e</sup>K. Nishi and T. Suzuki (unpublished)

<sup>f</sup>A. Gomyo *et al.*, *Mater. Res. Symp. Proc.* **417**, 91 (1996)

<sup>g</sup>A. Gomyo *et al.*, *Phys. Rev. Lett.* **60**, 2645 (1988)

<sup>h</sup>T. Suzuki *et al.*, *Appl. Phys. Lett.* **73**, 2588 (1998)

<sup>i</sup>A. G. Norman *et al.*, *Inst. Phys. Conf. Ser.* **87**, 77 (1987)

<sup>j</sup>M. A. Shahid *et al.*, *Phys. Rev. Lett.* **58**, 2567 (1987)

<sup>k</sup>T.-Y. Seong *et al.*, *J. Appl. Phys.* **75**, 7852 (1994)

<sup>l</sup>J. Shin *et al.*, *J. Electron. Mater.* **24**, 1563 (1995)

<sup>m</sup>G. S. Chen *et al.*, *Appl. Phys. Lett.* **57**, 2475 (1990)

<sup>n</sup>G. B. Stringfellow, *J. Cryst. Growth* **98**, 108 (1989)

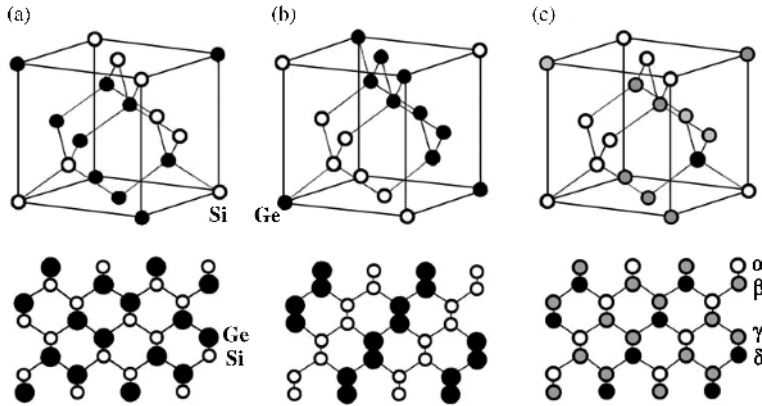


**Figure 1.2** Si–Ge ordered structures of types (a) RS1, (b) RS2 and (c) RS3. In (c), the four projected compositions  $\alpha$ ,  $\beta$ ,  $\gamma$  and  $\delta$  correspond to specific Si- and Ge-rich sites

Normally,  $\text{Si}_x\text{Ge}_{1-x}$  crystallizes in the diamond structure which contains of two fcc sublattices shifted by one quarter of the body diagonal. Observations of long-range ordering of group-IV semiconductor alloy have been made on  $\text{Si}_x\text{Ge}_{1-x}$  layers grown on Si(100) by MEB [3] and subsequently at interfaces of SLs [2]. Different order structures were suggested in bulk  $\text{Si}_x\text{Ge}_{1-x}$  on the basis of experimental results and are depicted in Figure 1.2. They are RS1, RS2 and RS3 with the rhombohedral structures (CuPt ordering,  $R3m$ ). The stoichiometry for RS1 and RS2 is  $\text{Si}_{0.5}\text{Ge}_{0.5}$ , while RS3 allows compositional differences on specific lattice sites. As seen in Figure 1.2, RS1 (RS2) has the widely (closely) spaced  $\{111\}$  planes occupied by the same atom type, while RS3 allows compositional differences between projected sites or columns with compositions  $\alpha$ ,  $\beta$ ,  $\gamma$  and  $\delta$  corresponding to specific Si- and Ge-rich sites.

<sup>o</sup>Y.-E. Ihm *et al.*, *Appl. Phys. Lett.* **51**, 2013 (1987)

<sup>p</sup>D. H. Jaw *et al.*, *Appl. Phys. Lett.* **59**, 114 (1991)

<sup>q</sup>See, H. R. Jen *et al.*, *Appl. Phys. Lett.* **54**, 1890 (1989)

<sup>r</sup>H. R. Jen *et al.*, *Appl. Phys. Lett.* **54**, 1154 (1989)

<sup>s</sup>T.-Y. Seong *et al.*, *Appl. Phys. Lett.* **64**, 3593 (1994)

<sup>t</sup>W. E. Plano *et al.*, *Appl. Phys. Lett.* **53**, 2537 (1988)

<sup>u</sup>T. Suzuki *et al.*, *Appl. Phys. Lett.* **73**, 2588 (1998)

<sup>v</sup>T. S. Kuan *et al.*, *Phys. Rev. Lett.* **54**, 201 (1985)

<sup>w</sup>O. Ueda, *et al.*, *J. Cryst. Growth* **115**, 375 (1991)

<sup>x</sup>O. Ueta *et al.*, *Proc. 7th Int. Conf. InP and Related Materials Sapporo*, Japan, p. 253 (1995)

<sup>y</sup>H. R. Jen *et al.*, *Appl. Phys. Lett.* **48**, 1603 (1986)

<sup>z</sup>A. Gomyo *et al.*, *Phys. Rev. Lett.* **72**, 673 (1994)

<sup>aa</sup>D. Shindo *et al.*, *J. Electron Microscopy* **45**, 99 (1996)

<sup>ab</sup>N. Amir *et al.*, *J. Phys. D: Appl. Phys.* **33**, L9 (2000)

<sup>ac</sup>K. T. Chang and E. Goo, *J. Vac. Sci. Technol. B* **10**, 1549 (1992)

<sup>ad</sup>K. Wolf *et al.*, *Solid State Commun.* **94**, 103 (1995)

<sup>ae</sup>H. S. Lee *et al.*, *Appl. Phys. Lett.* **83**, 896 (2003)

<sup>af</sup>H. Luo *et al.*, *J. Vac. Sci. Technol. B* **12**, 1140 (1994)

<sup>ag</sup>H. S. Lee *et al.*, *Solid State Commun.* **137**, 70 (2006)

The long-range order parameter in RS1 and RS2 can be defined by

$$S = \frac{r_{\text{Si}} - x}{1 - x} \quad (1.2)$$

where  $r_{\text{Si}}$  is the fraction of Si sites occupied correctly and  $x$  is the fraction of Si atoms in  $\text{Si}_x\text{Ge}_{1-x}$ .  $S = 1$  means perfect and complete order, while  $S = 0$  means random alloy. The degree of long-range order can be quantitatively deduced from the electron diffraction intensity of superstructure reflections. However, because of the presence of crystalline defects, of superposition of various domains and of the multiple scattering, the actual intensity substantially deviates from the kinematic value so that quantitative determination from selected-area electron diffraction intensity is usually obscured [2].

Observations of the long-range ordering have been made on bulk SiGe or SL samples prepared by MBE at medium temperature and for various compositions. However, no observations of ordered phases are reported for bulk SiGe grown from the melt [4].

### (b) III-V semiconductor alloy

In 1985, Kuan *et al.* [5] first observed an ordered phase (CuAu-I type) in III-V semiconductor alloy which was an AlGaAs epilayer grown on GaAs(100) at 600–800 °C by MOCVD. Since the finding of CuPt-type ordering in SiGe alloy [3], this type of ordering (CuPt-B) has also been reported for many III-V alloys, such as AlInP, GaInP, AlInAs and GaInAs ([6], see also Table 1.3). New types of ordering, CuPt-A and TP-A, are also found in AlInP [7] and AlInAs alloys [8]. Other types of ordering, CuAu-I, famatinite and chalcopyrite, are reported in the early history of the spontaneous ordering in III-V alloys; however, mechanism of these phases seems to be quite different from those of CuPt-B, CuPt-A and TP-A [6].

The unit cells of (a) CuPt-B, (b) CuAu-I and (c) chalcopyrite structures are shown in Figure 1.3. The metallurgical CuPt alloy has a random fcc structure at high temperatures, but quenching at low temperatures produces a rhombohedral phase with  $1/2\{111\}$  chemical ordering. The CuPt-B structure is among the most widely discussed and accessed forms of spontaneous ordering in III-V ternaries, and occurs in both common anion and common cation alloys (Table 1.3). It is a monolayer SL of  $\text{III}_A$  ( $V_A$ )-rich planes and  $\text{III}_B$  ( $V_B$ )-rich planes ordered in the  $[\bar{1}11]$  or  $[1\bar{1}1]$  directions, as depicted in Figure 1.4. The CuPt-A and

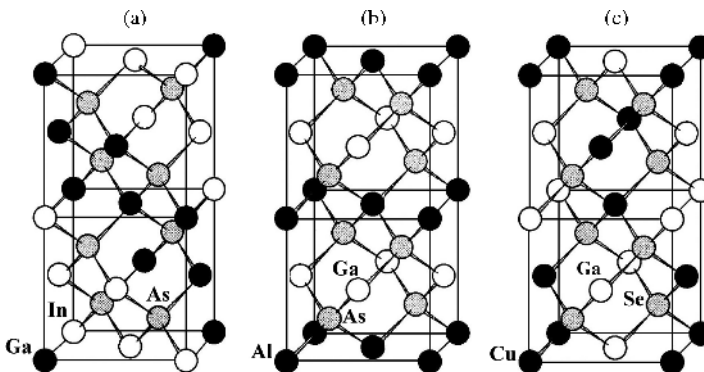


**Figure 1.3** Unit cells of (a) CuPt-B (GaInAs), (b) CuAu-I (AlGaAs) and (c) chalcopyrite structures (CuGaSe<sub>2</sub>)

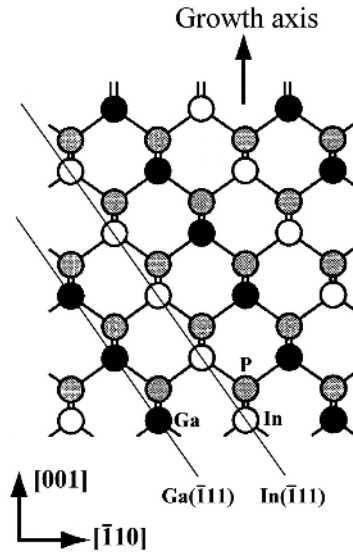


**Figure 1.4**  $[110]$  projection of CuPt-B ordering (GaInP)

TP-A phases occur in the  $[\bar{1}\bar{1}\bar{1}]$  and  $[11\bar{1}]$  directions, in which CuPt-B ordering is never observed. The metallic CuAu alloy shows two prominent ordered phases: (i) CuAu-I trigonal phase with alternating (002) planes of pure Cu and Au compositions and (ii) orthorhombic CuAu-II phase. The CuAu-I ordering occurs spontaneously within fcc sublattices of some III–V pseudobinary alloys, such as AlGaAs, GaInAs and GaAsSb (Table 1.3).

An earlier thermodynamic calculation based on a first-principles theory predicted that an ordered phase with a large lattice-constant mismatch is more stable than the corresponding random phase [9]. Some experimental data, on the other hand, showed that the kinetics of crystal growth plays an important role in the formation of an ordered structure as discussed in Mascarenhas [2].

### (c) II–VI semiconductor alloy

Only a few studies have been carried out on spontaneous ordering of II–VI semiconductor alloys. These studies reported ordering of CuPt and CuAu-I types (Table 1.3). Recently, a new ordering phase,  $\text{Cu}_3\text{Au}$ , has been observed in  $\text{Zn}_{0.9}\text{Cd}_{0.1}\text{Te}$  epilayers grown on GaAs(100) substrates [10]. We can see a tendency in Table 1.3 to observe the CuPt (CuAu-I) phase if samples were grown by MOCVD (MBE).

## 1.4 LATTICE CONSTANT AND RELATED PARAMETERS

### 1.4.1 CuAu Alloy: Ordered and Disordered States

Cu–Au alloy is among the best studied of all metallic alloys. The most interesting feature of this alloy is that CuAu ( $x = 0.5$ ),  $\text{CuAu}_3$  ( $x = 0.25$ ) and  $\text{Cu}_3\text{Au}$  ( $x = 0.75$ ) can be obtained in either ordered or disordered form. The ordered CuAu alloy crystallizes in the  $\text{Ll}_0$  tetragonal structure

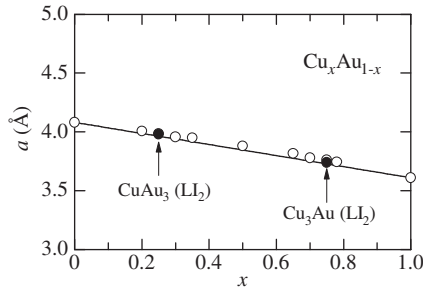


**Figure 1.5** Lattice constant  $a$  versus  $x$  for  $\text{Cu}_x\text{Au}_{1-x}$ . The solid and open circles represent the ordered ( $x = 0.25, 0.75$ ) and disordered alloy values, respectively. The solid line shows the linear interpolation result between the endpoint elemental data

(space group =  $P4/mmm$ ), while the ordered  $\text{CuAu}_3$  and  $\text{Cu}_3\text{Au}$  alloys crystallize in the  $\text{LI}_2$  cubic structure ( $Pm\bar{3}m$ ).

In Figure 1.5 the lattice constant  $a$  has been plotted as a function of  $x$  for  $\text{Cu}_x\text{Au}_{1-x}$ . The solid and open circles represent the ordered and disordered alloy data, respectively. The solid line shows the linear interpolation result between the Au ( $x = 0$ ) and Cu ( $x = 1.0$ ) values. It can be seen from Figure 1.5 that the Cu–Au ordering has no strong effect on the lattice parameter. Similarly, no clear spontaneous ordering effect has been observed on the lattice parameters of semiconductor alloys.

### 1.4.2 Non-alloyed Semiconductor

The lattice parameters for a number of the most easily grown group-IV, III–V and II–VI semiconductors are listed in Table 1.4. Tables 1.5, 1.6 and 1.7 also list the molecular weight ( $M$ ), lattice constants ( $a$  and  $b$ ) and crystal density ( $\rho$ ) for a number of group-IV, III–V and II–VI semiconductors crystallizing in the diamond, zinc-blende and wurtzite structures, respectively. These values can be used to obtain alloy values using the interpolation scheme.

**Table 1.4** Most easily grown crystal structure and lattice constants at 300 K for a number of easily or normally grown group-IV, III–V and II–VI semiconductors. d = diamond; zb = zinc-blende; h = hexagonal; w = wurtzite; rs = rocksalt; or = orthorhombic; rh = rhombohedral

System	Material	Crystal structure	$a$ (Å)	$c$ (Å)
IV	Diamond	d	3.5670	
	Si	d	5.4310	
	Ge	d	5.6579	
	Sn	d	6.4892	
	3C-SiC	zb	4.3596	
	6H-SiC	h	3.0806	15.1173

**Table 1.4** (Continued)

System	Material	Crystal structure	$a$ (Å)	$c$ (Å)	
III-V	BN	zb	3.6155		
	BN	h	2.5040	6.6612	
	BP	zb	4.5383		
	BAs	zb	4.777		
	AlN	h (w)	3.112	4.982	
	AlP	zb	5.4635		
	AlAs	zb	5.66139		
	AlSb	zb	6.1355		
	GaN	h (w)	3.1896	5.1855	
	GaP	zb	5.4508		
	GaAs	zb	5.65330		
	GaSb	zb	6.09593		
	InN	h (w)	3.548	5.760	
	InP	zb	5.8690		
	InAs	zb	6.0583		
InSb	zb	6.47937			
II-VI	BeO	h (w)	2.6979	4.380	
	BeS	zb	4.865		
	BeSe	zb	5.137		
	BeTe	zb	5.617		
	MgO	rs	4.203		
	MgS	rs	5.203		
	MgSe	zb	5.91		
	MgTe	h (w)	4.548	7.390	
	ZnO	h (w)	3.2495	5.2069	
	ZnS	h (w)	3.8226	6.2605	
	ZnS	zb	5.4102		
	ZnSe	zb	5.6692		
	ZnTe	zb	6.1037		
	CdO	rs	4.686		
	CdS	h (w)	4.1367	6.7161	
	CdSe	h (w)	4.2999	7.0109	
	CdTe	zb	6.481		
	HgO		or	3.577 ( <i>a</i> )	
				8.681 ( <i>b</i> )	
				2.427 ( <i>c</i> )	
				0.745 ( <i>u</i> )	
				4.14 ( <i>a</i> )	
				9.49 ( <i>b</i> )	
2.292 ( <i>c</i> )					
HgS	rh		0.720 ( <i>u</i> )		
			0.480 ( <i>v</i> )		
			6.084		
			6.4603		
HgSe	zb	6.084			
HgTe	zb	6.4603			

**Table 1.5** Molecular weight  $M$ , lattice constant  $a$  and crystal density  $g$  for a number of cubic, diamond-type semiconductors at 300 K

System	Material	$M$ (amu)	$a$ (Å)	$g$ (g/cm <sup>3</sup> )
IV	Diamond	12.0107	3.5670	3.5156
	Si	28.0855	5.4310	2.3291
	Ge	72.61	5.6579	5.3256
	Sn	118.710	6.4892	5.7710

**Table 1.6** Molecular weight  $M$ , lattice constant  $a$  and crystal density  $g$  for a number of cubic, zinc-blende-type semiconductors at 300 K

System	Material	$M$ (amu)	$a$ (Å)	$g$ (g/cm <sup>3</sup> )
IV	3C-SiC	40.0962	4.3596	3.2142
III-V	BN	24.818	3.6155	3.4880
	BP	41.785	4.5383	2.9693
	BAs	85.733	4.777	5.224
	AlN	40.98828	4.38	3.24
	AlP	57.955299	5.4635	2.3604
	AlAs	101.903098	5.66139	3.73016
	AlSb	148.742	6.1355	4.2775
	GaN	83.730	4.52	6.02
	GaP	100.696	5.4508	4.1299
	GaAs	144.645	5.65330	5.31749
	GaSb	191.483	6.09593	5.61461
	InN	128.825	4.986	6.903
	InP	145.792	5.8690	4.7902
	InAs	189.740	6.0583	5.6678
InSb	236.578	6.47937	5.77677	
II-VI	BeO	25.0116	3.80	3.03
	BeS	41.078	4.865	2.370
	BeSe	87.97	5.137	4.310
	BeTe	136.61	5.617	5.120
	MgO	40.3044	4.21	3.59
	MgS	56.371	5.62	2.11
	MgSe	103.27	5.91	3.32
	MgTe	151.91	6.42	3.81
	ZnO	81.39	4.47	6.05
	ZnS	97.46	5.4102	4.0879
	ZnSe	144.35	5.6692	5.2621
	ZnTe	192.99	6.1037	5.6372
	CdO	128.410	5.148 <sup>a</sup>	6.252 <sup>a</sup>
	CdS	144.477	5.825	4.855
	CdSe	191.37	6.077	5.664
	CdTe	240.01	6.481	5.856
	HgS	232.66	5.8514	7.7135
	HgSe	279.55	6.084	8.245
HgTe	328.19	6.4603	8.0849	

<sup>a</sup>Theoretical

**Table 1.7** Molecular weight  $M$ , lattice constants  $a$  and  $c$  and crystal density  $g$  for a number of hexagonal, wurtzite-type semiconductors at 300 K

System	Material	$M$ (amu)	Lattice constant (Å)		$g$ (g/cm <sup>3</sup> )
			$a$	$c$	
IV	2H-SiC	40.0962	3.0763	5.0480	3.2187
III-V	AlN	40.98828	3.112	4.982	3.258
	GaN	83.730	3.1896	5.1855	6.0865
	InN	128.825	3.548	5.760	6.813
II-VI	BeO	25.0116	2.6979	4.380	3.009
	BeS <sup>a</sup>	41.078	3.440	5.618	2.370
	BeSe <sup>a</sup>	87.97	3.632	5.932	4.311
	BeTe <sup>a</sup>	136.61	3.972	6.486	5.120
	MgO	40.3044	3.199	5.086	2.970
	MgS	56.371	3.972	6.443	2.127
	MgSe	103.27	4.145	6.723	3.429
	MgTe	151.91	4.548	7.390	3.811
	ZnO	81.39	3.2495	5.2069	5.6768
	ZnS	97.46	3.8226	6.2605	4.0855
	ZnSe	144.35	3.996	6.626	5.232
	ZnTe	192.99	4.27	6.99	5.81
	CdO <sup>a</sup>	128.410	3.678	5.825	6.249
	CdS	144.477	4.1367	6.7161	4.8208
	CdSe	191.37	4.2999	7.0109	5.6615
	CdTe	240.01	4.57	7.47	5.90
	HgS <sup>a</sup>	232.66	4.1376	6.7566	7.7134
	HgSe <sup>a</sup>	279.55	4.302	7.025	8.246
	HgTe <sup>a</sup>	328.19	4.5681	7.4597	8.0850

<sup>a</sup>Estimated or theoretical

### 1.4.3 Semiconductor Alloy

#### (a) Group-IV semiconductor

Table 1.8 gives the lattice-matching condition between some group-IV ternary alloys and Si substrate. The incorporation of carbon into Si or SiGe gives rise to additional flexibility for group-IV-based heterostructure design [11]. Due to huge lattice mismatch between diamond

**Table 1.8** Lattice-matching conditions of some group-IV ternaries at 300 K

Material	Substrate	Expression	Remark
C <sub>x</sub> Si <sub>y</sub> Ge <sub>1-x-y</sub>	Si	$x = 0.109 - 0.109y$	$0 \leq y \leq 1.0, x/(1-x-y) = 0.122$
C <sub>x</sub> Si <sub>y</sub> Sn <sub>1-x-y</sub>	Si	$x = 0.362 - 0.362y$	$0 \leq y \leq 1.0, x/(1-x-y) = 0.567$
C <sub>x</sub> Ge <sub>y</sub> Sn <sub>1-x-y</sub>	Si	$x = 0.362 - 0.284y$	$0 \leq y \leq 0.89$

and Si, a small amount of substantially incorporated C induces a substantial tensile strain in pseudomorphic  $C_xSi_{1-x}$  layers on Si. This effect can be exploited for  $C_xSi_yGe_{1-x-y}/Si$ ,  $C_xSi_ySn_{1-x-y}/Si$  and  $C_xGe_ySn_{1-x-y}/Si$  heterostructures by properly choosing pseudomorphic compositions  $x$  and  $y$ . It should be noted, however, that the solubility of C into Si is only about  $6 \times 10^{-6}$  at% ( $\sim 3 \times 10^{-17} \text{ cm}^{-3}$ ) at the melting point of Si. Carbon incorporated into substitutional lattice sites up to a few atomic percent has been achieved only using growth techniques far from thermodynamic equilibrium [12].

Figure 1.6 shows the plot of the lattice constant  $a$  versus  $x$  for bulk  $C_xSi_{1-x}$ . The open circles represent the experimental data for diamond and Si, while the solid circle shows the data for

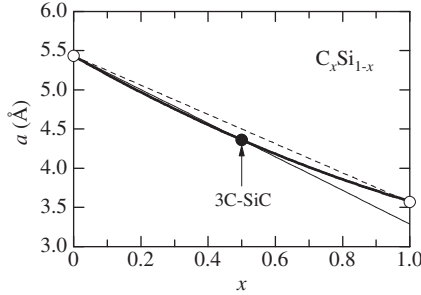


**Figure 1.6** Lattice constant  $a$  versus  $x$  for bulk  $C_xSi_{1-x}$  at 300 K. The open and solid circles represent the experimental data. The light solid and dashed lines represent the results of Vegard law between Si ( $x=0$ ) and 3C-SiC ( $x=0.5$ ) and between Si ( $x=0$ ) and diamond ( $x=1.0$ ), respectively. The heavy solid line shows the theoretical values obtained from a Monte Carlo simulation by Kelires [13]

3C-SiC ( $x=0.5$ ). The light solid line is obtained from Vegard law between Si and 3C-SiC ( $x=0.5$ ), while the dashed line is obtained between Si and diamond ( $x=1.0$ ). The 3C-SiC value is smaller than the linearly interpolated value. The heavy solid line in Figure 1.6 represents the theoretical  $a$  values for  $C_xSi_{1-x}$  obtained from a Monte Carlo calculation [13]. These values can be expressed as (in Å)

$$a(x) = 5.4310 - 2.4239x + 0.5705x^2 \quad (1.3)$$

The negative deviation  $a(x)$  seen in Figure 1.6 has been confirmed experimentally from pseudomorphic  $C_xSi_{1-x}$  epilayers ( $x < 0.012$ ) grown on Si(100) by solid-source MBE [14].

Si and Ge, both crystallize in the diamond structure, form a continuous series of  $Si_xGe_{1-x}$  alloys with  $x$  ranging from 0 to 1.0. The most precise and comprehensive determination of the lattice constant  $a$  and crystal density  $g$  across the whole alloy range was undertaken by Dismukes *et al.* [15]. The values they obtained for  $a$  and  $g$  are plotted versus  $x$  for  $Si_xGe_{1-x}$  in Figure 1.7. These data reveal a small deviation from Vegard law, i.e. from the linearity between the endpoint values. The lattice parameter  $a$  shows a downward bowing, while the density parameter  $g$  gives an upward bowing. From Figure 1.7, we obtain parabolic relation for  $a$  and  $g$  as a function of  $x$  ( $a$  in Å,  $g$  in  $\text{g/cm}^3$ )

$$a(x) = 5.6575 - 0.2530x + 0.0266x^2 \quad (1.4a)$$

$$g(x) = 5.3256 - 2.5083x - 0.4853x^2 \quad (1.4b)$$

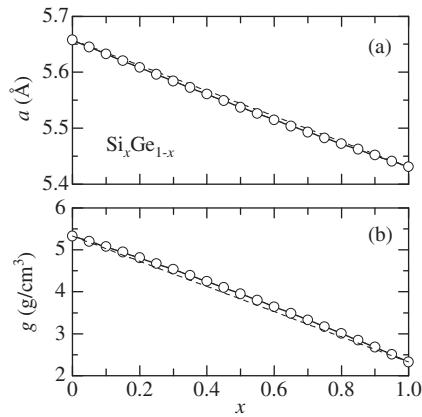


**Figure 1.7** (a) Lattice constant  $a$  and (b) crystal density  $g$  for  $\text{Si}_x\text{Ge}_{1-x}$  at 300 K. The experimental data are taken from Dismukes *et al.* [15]. The solid and dashed lines represent the parabolic and linear fit results, respectively

As shown in Figure 1.8, the diamond-type lattice, e.g. Si has only one type of first-neighbor distance

$$d(\text{Si}-\text{Si}) = \frac{\sqrt{3}}{4} a \text{ (four bonds)} \quad (1.5)$$

EXAFS has been popularly used to determine bond lengths for different types of neighbor atom pairs and the corresponding fractional occupancy of each type of neighbor. Recent EXAFS and XRD studies performed on strained  $\text{Si}_x\text{Ge}_{1-x}/\text{Si}$  layers indicated that the Si-Si, Si-Ge and Ge-Ge nearest-neighbor distances are  $2.35 \pm 0.02$ ,  $2.42 \pm 0.02$  and  $2.38 \pm 0.02$  Å, respectively, close to the sum of their constituent-element covalent radii and independent of  $x$ , while the lattice constant varies monotonically with  $x$  [16,17]. More recently, Yonenaga *et al.* [18] investigated the local atomistic structure in bulk Czochralski-grown  $\text{Si}_x\text{Ge}_{1-x}$  using EXAFS. As shown in Figure 1.9, the bond lengths Si-Si, Si-Ge and Ge-Ge in the bulk  $\text{Si}_x\text{Ge}_{1-x}$  remain distinctly different lengths and vary in linear fashion of  $x$  over the entire composition range  $0 \leq x \leq 1.0$ , in agreement with expectation derived from *ab-initio* electronic structure calculation. These results suggest that  $\text{Si}_x\text{Ge}_{1-x}$  is a typical disorder material and that the bond lengths and bond angles are disordered with  $x$  in  $\text{Si}_x\text{Ge}_{1-x}$ .

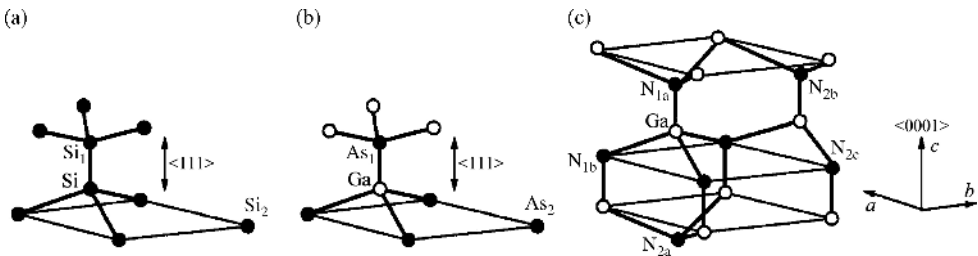


**Figure 1.8** Bond distances in (a) diamond (Si), (b) zinc-blende (GaAs) and (c) wurtzite structures (GaN)

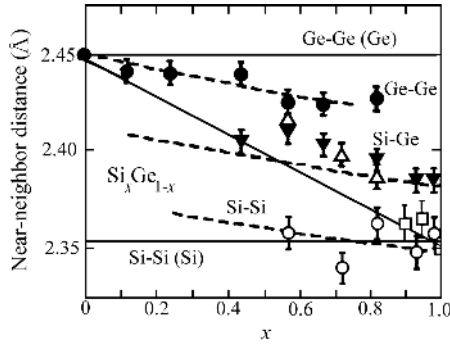


**Figure 1.9** Near-neighbor distance in  $\text{Si}_x\text{Ge}_{1-x}$  at 300 K. The experimental data are taken from Yonenaga *et al.* [18]. The horizontal lines show the bond lengths in bulk Si and Ge. The middle thin line is obtained from Vegard law

**(b) III–V semiconductor**

The expressions for  $a$  versus alloy composition can be obtained from Vegard law. The crystal density can also be calculated from  $g = Md_M/N_A$ , where  $M$  is the molecular weight,  $N_A = 6.022 \times 10^{23} \text{ mol}^{-1}$  is the Avogadro constant and  $d_M$  is the molecular density [1].

The III–V quaternaries can be epitaxially grown on some III–V binaries (GaAs, InP, etc.). Introducing the binary lattice parameters in Table 1.6 into Equation (A.6) or Equation (A.8), we can obtain the lattice-matching conditions for  $A_x\text{B}_{1-x}\text{C}_y\text{D}_{1-y}$  and  $A_x\text{B}_y\text{C}_{1-x-y}\text{D}$  quaternaries on various III–V binary substrates. These results are summarized in Tables 1.9–1.11. The lattice-matching conditions in Tables 1.9–1.11 can be approximated by more simple expressions. Some results are presented in Table 1.12.

The lattice parameter  $a$  at 300 K as a function of  $x$  for  $\text{Al}_x\text{Ga}_{1-x}\text{As}$  is shown in Figure 1.10. The experimental data are taken from Takahashi [19]. From a least-squares fit, we obtain

$$a(x) = 5.6533 + 0.0083x - 0.0003x^2 \quad (1.6)$$

The solid line in Figure 1.10 shows the calculated result of Equation (1.6). This equation promises that the lattice parameter for  $\text{Al}_x\text{Ga}_{1-x}\text{As}$  can be given by Vegard law with good

**Table 1.9** Lattice-matching conditions for some cubic, zinc-blende-type III–V quaternaries of type  $A_x\text{B}_{1-x}\text{C}_y\text{D}_{1-y}$  at 300 K

$$x = \frac{A_0 + B_0y}{C_0 + D_0y}$$

Quaternary	Substrate	$A_0$	$B_0$	$C_0$	$D_0$	Remark
$\text{Al}_x\text{In}_{1-x}\text{P}_y\text{As}_{1-y}$	GaAs	0.4050	-0.1893	0.3969	0.0086	$0.04 \leq y \leq 1.0$
	InP	0.1893	-0.1893	0.3969	0.0086	$0 \leq y \leq 1.0$
$\text{Ga}_x\text{In}_{1-x}\text{P}_y\text{As}_{1-y}$	GaAs	0.4050	-0.1893	0.4050	0.0132	$0 \leq y \leq 1.0$
	InP	0.1893	-0.1893	0.4050	0.0132	$0 \leq y \leq 1.0$

**Table 1.10** Lattice-matching conditions for some cubic, zinc-blende-type III–V quaternaries of type  $A_xB_{1-x}C_yD_{1-y}$  at 300 K

$$y = \frac{A_0 + B_0x}{C_0 + D_0x}$$

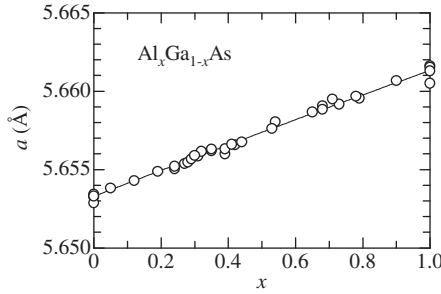
Quaternary	Substrate	$A_0$	$B_0$	$C_0$	$D_0$	Remark
$Al_xGa_{1-x}P_yAs_{1-y}$	GaAs	0	0.0081	0.2025	-0.0046	$0 \leq x \leq 1.0$
$Al_xGa_{1-x}P_ySb_{1-y}$	GaAs	0.4426	0.0396	0.6451	0.0269	$0 \leq x \leq 1.0$
	GaSb	0	0.0396	0.6451	0.0269	$0 \leq x \leq 1.0$
	InP	0.2269	0.0396	0.6451	0.0269	$0 \leq x \leq 1.0$
	InAs	0.0376	0.0396	0.6451	0.0269	$0 \leq x \leq 1.0$
$Al_xGa_{1-x}As_ySb_{1-y}$	GaSb	0	0.0396	0.4426	0.0315	$0 \leq x \leq 1.0$
	InP	0.2269	0.0396	0.4426	0.0315	$0 \leq x \leq 1.0$
	InAs	0.0376	0.0396	0.4426	0.0315	$0 \leq x \leq 1.0$
$Al_xIn_{1-x}P_ySb_{1-y}$	GaAs	0.8261	-0.3439	0.6104	0.0616	$0.53 \leq x \leq 1.0$
	GaSb	0.3834	-0.3439	0.6104	0.0616	$0 \leq x \leq 1.0$
	InP	0.6104	-0.3439	0.6104	0.0616	$0 \leq x \leq 1.0$
	InAs	0.4211	-0.3439	0.6104	0.0616	$0 \leq x \leq 1.0$
$Al_xIn_{1-x}As_ySb_{1-y}$	GaSb	0.3834	-0.3439	0.4211	0.0530	$0 \leq x \leq 1.0$
	InP	0.6104	-0.3439	0.4211	0.0530	$0.48 \leq x \leq 1.0$
	InAs	0.4211	-0.3439	0.4211	0.0530	$0 \leq x \leq 1.0$
$Ga_xIn_{1-x}P_ySb_{1-y}$	GaAs	0.8261	-0.3834	0.6104	0.0348	$0.52 \leq x \leq 1.0$
	GaSb	0.3834	-0.3834	0.6104	0.0348	$0 \leq x \leq 1.0$
	InP	0.6104	-0.3834	0.6104	0.0348	$0 \leq x \leq 1.0$
	InAs	0.4211	-0.3834	0.6104	0.0348	$0 \leq x \leq 1.0$
$Ga_xIn_{1-x}As_ySb_{1-y}$	GaSb	0.3834	-0.3834	0.4211	0.0216	$0 \leq x \leq 1.0$
	InP	0.6104	-0.3834	0.4211	0.0216	$0.47 \leq x \leq 1.0$
	InAs	0.4211	-0.3834	0.4211	0.0216	$0 \leq x \leq 1.0$

**Table 1.11** Lattice-matching conditions for some cubic, zinc-blende-type III–V quaternaries of the type  $A_xB_yC_{1-x-y}D$  or  $AB_xC_yD_{1-x-y}$  at 300 K

Quaternary	Substrate	Expression	Remark
$Al_xGa_yIn_{1-x-y}P$	GaAs	$y = 0.5158 - 0.9696x$	$0 \leq x \leq 0.53$
$Al_xGa_yIn_{1-x-y}As$	InP	$y = 0.4674 - 0.9800x$	$0 \leq x \leq 0.48$
$AlP_xAs_ySb_{1-x-y}$	GaAs	$x = 0.7176 - 0.7055y$	$0 \leq y \leq 1.0$
	InP	$x = 0.3966 - 0.7055y$	$0 \leq y \leq 0.56$
	InAs	$x = 0.1149 - 0.7055y$	$0 \leq y \leq 0.16$
$GaP_xAs_ySb_{1-x-y}$	GaAs	$x = 0.6861 - 0.6861y$	$0 \leq y \leq 1.0$
	InP	$x = 0.3518 - 0.6861y$	$0 \leq y \leq 0.51$
	InAs	$x = 0.0583 - 0.6861y$	$0 \leq y \leq 0.08$
$InP_xAs_ySb_{1-x-y}$	GaSb	$x = 0.6282 - 0.6899y$	$0 \leq y \leq 0.91$
	InAs	$x = 0.6899 - 0.6899y$	$0 \leq y \leq 1.0$

**Table 1.12** Approximated lattice-matching expression for some important cubic, zinc-blende-type III–V quaternaries at 300 K

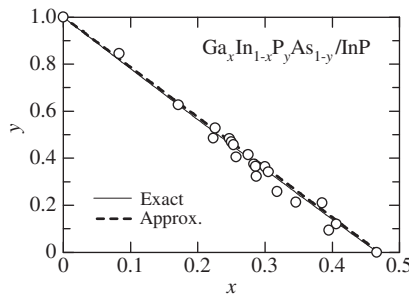
Quaternary	Substrate	Expression	Remark
$\text{Al}_x\text{Ga}_{1-x}\text{As}_y\text{Sb}_{1-y}$	GaSb	$y = 0.084x$	$0 \leq x \leq 1.0$
	InAs	$y = 0.085 + 0.078x$	$0 \leq x \leq 1.0$
$\text{Ga}_x\text{In}_{1-x}\text{P}_y\text{As}_{1-y}$	InP	$x = 0.47 - 0.47y$	$0 \leq y \leq 1.0$
	GaSb	$y = 0.91 - 0.91x$	$0 \leq x \leq 1.0$
$\text{Al}_x\text{Ga}_y\text{In}_{1-x-y}\text{P}$	InAs	$y = 1.00 - 0.91x$	$0 \leq x \leq 1.0$
	GaAs	$y = 0.52 - 0.97x$	$0 \leq x \leq 0.53$
$\text{Al}_x\text{Ga}_y\text{In}_{1-x-y}\text{As}$	InP	$y = 0.47 - 0.98x$	$0 \leq x \leq 0.48$

**Figure 1.10** Lattice parameter  $a$  as a function of  $x$  for  $\text{Al}_x\text{Ga}_{1-x}\text{As}$  at 300 K. The experimental data are taken from Takahashi [19]. The solid line represents the quadratic least-squares fit

approximation. The difference in  $a$  between  $\text{Al}_x\text{Ga}_{1-x}\text{As}$  and GaAs can also be written as

$$\frac{a(\text{Al}_x\text{Ga}_{1-x}\text{As}) - a(\text{GaAs})}{a(\text{GaAs})} = 0.0015x = 0.15x\% \quad (1.7)$$

Figure 1.11 shows the experimental  $x$ – $y$  plots for  $\text{Ga}_x\text{In}_{1-x}\text{P}_y\text{As}_{1-y}/\text{InP}$  [20]. The solid line shows the exactly calculated  $x$ – $y$  relation in Table 1.9

**Figure 1.11** Plots of  $x$  versus  $y$  for  $\text{Ga}_x\text{In}_{1-x}\text{P}_y\text{As}_{1-y}$  nearly lattice-matched to InP at 300 K. The experimental data are taken from Nahory *et al.* [20]. The solid and dashed lines show the lattice-matching relationships obtained from Vegard law in Equations (1.8) and (1.9), respectively

$$x = \frac{0.1893 - 0.1893y}{0.4050 + 0.0132y} \quad (1.8)$$

The dashed line also shows the calculated result using an expression in Table 1.12

$$x = 0.47 - 0.47y \quad (1.9)$$

Both expressions can explain the experimental  $x$ - $y$  relation very well and simultaneously indicate the validity of Vegard law for  $\text{Ga}_x\text{In}_{1-x}\text{P}_y\text{As}_{1-y}/\text{InP}$ . It has, however, been reported that strained  $\text{Al}_x\text{Ga}_{1-x}\text{Sb}/\text{GaSb}$  does not obey Vegard law [21].

The crystal density  $g$  versus  $y$  for  $\text{Ga}_x\text{In}_{1-x}\text{P}_y\text{As}_{1-y}/\text{InP}$  is shown in Figure 1.12. The solid line represents the X-ray crystal density calculated from Equation (1.16) of Adachi [1], while the dashed line is obtained from the linear interpolation between the endpoint densities ( $y=0, 1.0$ ). Their difference is within 2%.

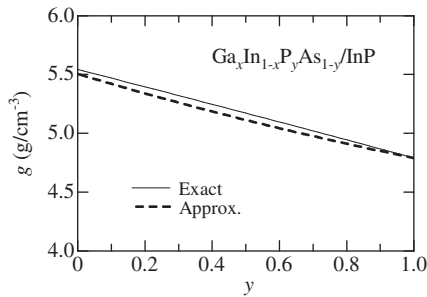


**Figure 1.12** X-ray crystal density  $g$  versus  $y$  for  $\text{Ga}_x\text{In}_{1-x}\text{P}_y\text{As}_{1-y}/\text{InP}$  at 300 K. The solid line represents the exact X-ray crystal density calculated from Equation (1.16) of Adachi [1], while the dashed line is obtained from the linear interpolation between the endpoint binary data

The experimental lattice parameter  $c$  as a function of  $x$  for  $w\text{-Ga}_x\text{In}_{1-x}\text{N}$  is plotted in Figure 1.13. The experimental data are taken from Bearch *et al.* [22] (solid circles) and Romano *et al.* [23] (open circles). The  $\text{Ga}_x\text{In}_{1-x}\text{N}$  layers ( $0 \leq x \leq 0.14$ ) used by Bearch *et al.* [22] were grown on (0001) sapphire by MOCVD and were believed to be fully relaxed. On the other hand, the  $\text{Ga}_x\text{In}_{1-x}\text{N}$  layers in Romano *et al.* [23] were pseudomorphically grown on 5  $\mu\text{m}$  thick GaN on (0001) sapphire by MOCVD ( $x=0-0.114$ ). The solid line in Figure 1.13 obeys Vegard law using  $c = 5.1855 \text{ \AA}$  for GaN and  $c = 5.760 \text{ \AA}$  for InN (Table 1.7).

Figure 1.14 shows the lattice parameter  $c$  versus  $x$  for strained  $\text{Al}_x\text{Ga}_{0.9-x}\text{In}_{0.1}\text{N}$  alloy grown by MOCVD [24]. The dashed line represents the linear interpolation result using the endpoint values taken from Table 1.7. The lattice parameter  $c$  is found to decrease almost linearly with increasing  $x$ . The prediction of Vegard law gives no good agreement with the experimental data.

It can be concluded from Figure 1.13 that the fully relaxed  $\text{Ga}_x\text{In}_{1-x}\text{N}$  films follow Vegard law well; however, no good agreement can be achieved in the case of the pseudomorphic alloy layers. As we will see later (Section 1.5.2), Vegard law may be applicable if any strain effects are artificially removed from such pseudomorphically strained layers.

HRXRD has been widely used and demonstrated that almost all III-V semiconductor alloys obey Vegard law well. It has also been reported that Vegard law remains valid in dilute nitrides, such as  $\text{GaN}_x\text{As}_{1-x}$  and  $\text{Ga}_x\text{In}_{1-x}\text{N}_y\text{As}_{1-y}$ , as long as all N atoms in the dilute nitrides locate at the arsenic sites [25]. The N-N pairs are thought to be the predominant N-related defects that cause deviation from Vegard law [26]. Germini *et al.* [21], however, observed a deviation

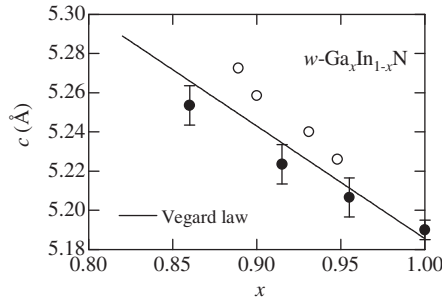


**Figure 1.13** Lattice parameter  $c$  as a function of  $x$  for  $w\text{-Ga}_x\text{In}_{1-x}\text{N}$  at 300 K. The experimental data are taken from Bearch *et al.* [22] (fully relaxed layers, solid circles) and Romano *et al.* [23] (pseudomorphic layers, open circles). The solid line represents the simply estimate of the  $c$  versus  $x$  relationship obtained from Vegard law

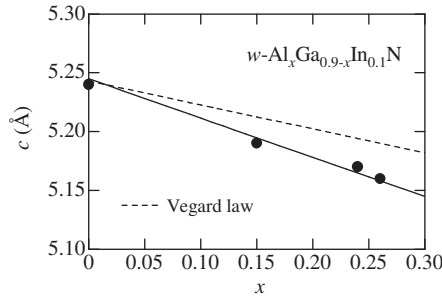


**Figure 1.14** Lattice parameter  $c$  versus  $x$  for strained  $w\text{-Al}_x\text{Ga}_{0.9-x}\text{In}_{0.1}\text{N}$  at 300 K. The experimental data are taken from Aumer *et al.* [24]. The dashed and solid lines represent the results of applying Vegard law before and after correcting for the biaxial strain effect

from Vegard law in MBE-grown  $\text{Al}_x\text{Ga}_{1-x}\text{Sb}/\text{GaSb}$  layers by HRXRD, RBS and RHEED. These results are plotted in Figure 1.15. The experimental unstrained lattice parameters can be described by

$$a(x) = 6.09593 + 0.04360x - 4.229 \times 10^{-3} x^2 \quad (1.10)$$

The deviation from linearity is found to be larger than the prediction of a perfect random alloy in the frame of the Fournet model [27].

There is a significant structural difference between the bond distance in the zinc-blende and wurtzite structures of  $\text{A}_x\text{B}_{1-x}\text{C}$  alloy. The first-neighbor distance in the zinc-blende structure is given from Figure 1.8 by

$$d(\text{Ga-As}) = \frac{\sqrt{3}}{4} a \text{ (four bonds)} \quad (1.11)$$

Yet, the wurtzite structure has two types of the first-neighbor anion-cation bond distances (Figure 1.8)

$$d(\text{Ga-N}_1) = ua \text{ (one bond)} \quad (1.12a)$$

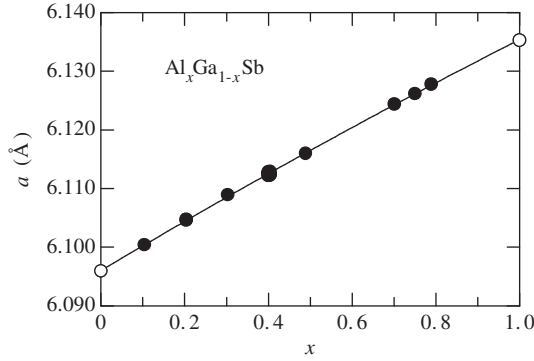


**Figure 1.15** Room-temperature lattice constant  $a$  as a function of  $x$  for  $\text{Al}_x\text{Ga}_{1-x}\text{Sb}$  grown on GaSb. The experimental data are taken from Germini *et al.* [21]. The solid line represents the quadratic best-fit result obtained using Equation (1.10)

$$d(\text{Ga}-\text{N}_2) = \sqrt{\frac{1}{3} + \left(\frac{1}{2} - u\right)^2 \left(\frac{c}{a_w}\right)^2} a_w \text{ (three bonds)} \quad (1.12b)$$

where  $u$  represents the cell-internal structural parameter and  $a_w$  and  $c$  show the lengths of the lattice vectors of the wurtzite structure. In the case of an ideal tetragonal ratio  $c/a_w = (8/3)^{1/2} = 1.6330$  and an ideal cell internal parameter  $u = 3/8$ , it follows from Equation (1.12) that  $d(\text{Ga}-\text{N}_1) = d(\text{Ga}-\text{N}_2)$ .

In the zinc-blende lattice, we have only one type of second neighbor cation–anion bond distance

$$d(\text{Ga}-\text{As}) = \frac{\sqrt{11}}{4} a \text{ (12 bonds)} \quad (1.13)$$

On the other hand, the wurtzite lattice has three types of second neighbor cation–anion distances concerning the cation A (Ga) to anions  $\text{C}_{2a}$ ,  $\text{C}_{2b}$  and  $\text{C}_{2c}$

$$d(\text{Ga}-\text{N}_{2a}) = (1-u) \frac{c}{a_w} a_w \text{ (one bond)} \quad (1.14a)$$

$$d(\text{Ga}-\text{N}_{2b}) = \sqrt{1 + \left(\frac{uc}{a_w}\right)^2} a_w \text{ (six bonds)} \quad (1.14b)$$

$$d(\text{Ga}-\text{N}_{2c}) = \sqrt{\frac{4}{3} + \left(\frac{1}{2} - u\right)^2 \left(\frac{c}{a_w}\right)^2} a_w \text{ (three bonds)} \quad (1.14c)$$

For ideal wurtzite parameters of  $c/a_w = (8/3)^{1/2} = 1.6330$  and  $u = 3/8$ , the following expression can be obtained from Equation (1.14)

$$d(\text{Ga}-\text{N}_{2a}) = 1.0206a_w, \quad d(\text{Ga}-\text{N}_{2b}) = d(\text{Ga}-\text{N}_{2c}) = 1.1726a_w \quad (1.15)$$

The spacing between the near-neighbor In–In or P–P atoms in InP is equal to  $(1/\sqrt{2})a$ . It would be anticipated that for an alloy the interatomic bond length of each constituent remains constant with alloy composition. Unfortunately, however, standard XRD techniques give information only on the lattice structure that is averaged over an area larger than the scale of

lattice constant. The interatomic structure in such semiconductor alloys was, therefore, not well understood until 1982. Mikkelsen and Boyce [28] reported in 1982 the interatomic structure of  $\text{Ga}_x\text{In}_{1-x}\text{As}$  using an EXAFS. They found that the Ga–As and In–As near-neighbor distances change by only 0.04 Å as the In composition varies from 1 to 99 at% despite the fact that this alloy accurately follows Vegard law with a change in average near-neighbor spacing of 0.17 Å. We reproduce in Figure 1.16 the results of Mikkelsen and Boyce [28]. They also observed that the cation sublattice approaches a virtual crystal (i.e. an average fcc lattice) with a broadened single distribution of second-neighbor distances, whereas the anion sublattice exhibits a bimodal anion–anion second-neighbor distribution.

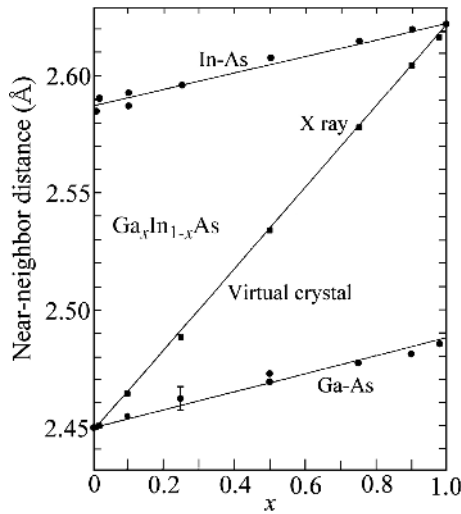


**Figure 1.16** Near-neighbor distance in  $\text{Ga}_x\text{In}_{1-x}\text{As}$  at 300 K. The middle thin line represents the bond length curve estimated from Vegard law. [Reprinted with permission from J. C. Mikkelsen, Jr. and J. B. Boyce, *Phys. Rev. Lett.* **49**, 1412 (1982). Copyright (1982) by the American Physical Society]

The essentially same EXAFS results, but on  $\text{Ga}_x\text{In}_{1-x}\text{P}_y\text{As}_{1-y}/\text{InP}$ , were reported by Oyanagi *et al.* [29]. They reported that the cation–anion distances in  $\text{Ga}_x\text{In}_{1-x}\text{P}_y\text{As}_{1-y}/\text{InP}$  deviate from the average interatomic distance, but are rather close to the bond lengths in pure parent crystals. The cation–anion distances obtained from this study are plotted in Figure 1.17.

The near-neighbor distances in  $w\text{-Ga}_x\text{In}_{1-x}\text{N}$  versus  $x$  are shown in Figure 1.18. The experimental data are taken from Jeffe *et al.* [30]. The theoretical lines are taken from Mattila and Zunger [31] in which the valence force field simulation with large supercells (512–1280 atoms) was used. It has been shown [31] that while the first-neighbor cation–anion bonds for different cations (Ga– $\text{N}_1$  and In– $\text{N}_1$ ) retain distinct values in the wurtzite and zinc-blende alloys, the second-neighbor cation–anion bonds Ga– $\text{N}_2$  and In– $\text{N}_2$  merge into a single bond length. However, the second-neighbor cation–anion bonds for the same cation exhibit a crucial difference between the wurtzite and zinc-blende structures. This is thought to be an intrinsic property of the binary constituents and persists in the alloy. The small splitting of the first-neighbor cation–anion bonds in the wurtzite structure is also preserved in the alloy, but obscured by bond length broadening [31].

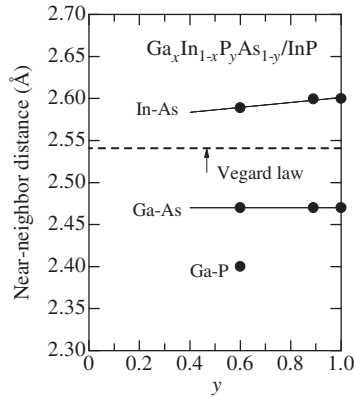


**Figure 1.17** Near-neighbor distance in  $\text{Ga}_x\text{In}_{1-x}\text{P}_y\text{As}_{1-y}/\text{InP}$  at 300 K. The experimental data are taken from Oyanagi *et al.* [29]. The dashed line represents the bond length curve obtained from Vegard law

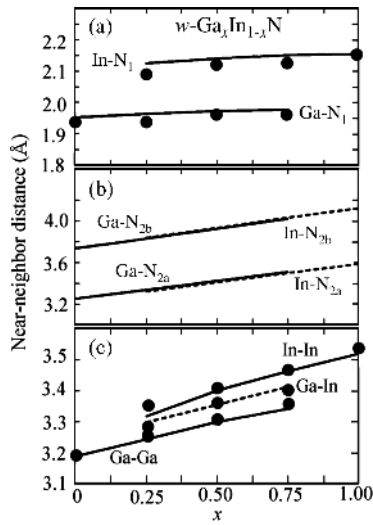


**Figure 1.18** Near-neighbor distances versus  $x$  for  $w\text{-Ga}_x\text{In}_{1-x}\text{N}$ . The experimental data were measured at 300 K by Jeffe *et al.* [30]. The theoretically calculated lines are taken from Mattila and Zunger [31] who used the valence force field simulation with large supercells (512–1280 atoms)

### (c) II–VI semiconductor

Several II–VI semiconductor quaternaries can be epitaxially grown on III–V binary substrates. The corresponding lattice-matching relationships are shown in Tables 1.13 and 1.14. These relationships can be approximated using more simple expressions, as listed in Table 1.15.

Figure 1.19 shows the lattice constant  $a$  as a function of  $x$  for  $\text{Zn}_x\text{Cd}_{1-x}\text{Te}$ . The experimental data were obtained at 300 K using an XRD combined with a WDXS [32]. The combination with WDXS led to an absolute composition error  $\Delta x$  of less than 0.01. These data suggest that Vegard

**Table 1.13** Lattice-matching conditions for some cubic, zinc-blende-type II–VI quaternaries of the type  $A_xB_{1-x}C_yD_{1-y}$  at 300 K

$$y = \frac{A_0 + B_0x}{C_0 + D_0x}$$

Quaternary	Substrate	$A_0$	$B_0$	$C_0$	$D_0$	Remark
$Mg_xZn_{1-x}S_ySe_{1-y}$	GaAs	0.016	0.241	0.259	0.031	$0 \leq x \leq 1.0$
$Mg_xZn_{1-x}Se_yTe_{1-y}$	InP	0.235	0.314	0.435	0.075	$0 \leq x \leq 0.84$

**Table 1.14** Lattice-matching conditions for some cubic, zinc-blende-type II–VI quaternaries of the type  $A_xB_yC_{1-x-y}D$  at 300 K

Quaternary	Substrate	Expression	Remark
$Be_xMg_yZn_{1-x-y}Se$	GaAs	$x = 0.030 + 0.453y$	$0 \leq y \leq 0.67$
$Mg_xZn_yCd_{1-x-y}Se$	InP	$y = 0.510 - 0.409x$	$0 \leq x \leq 0.83$

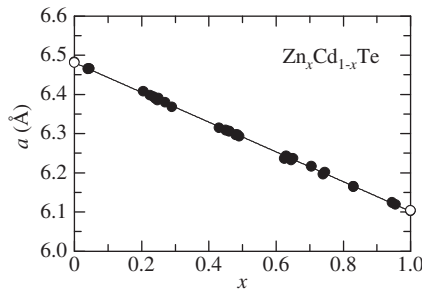
**Table 1.15** Approximated lattice-matching expression for some important cubic, zinc-blende-type II–VI quaternaries at 300 K

Quaternary	Substrate	Expression	Remark
$Mg_xZn_{1-x}S_ySe_{1-y}$	GaAs	$y = 0.08 + 0.82x$	$0 \leq x \leq 1.0$
$Mg_xZn_{1-x}Se_yTe_{1-y}$	InP	$y = 0.55 + 0.54x$	$0 \leq x \leq 0.84$
$Be_xMg_yZn_{1-x-y}Se$	GaAs	$x = 0.03 + 0.45y$	$0 \leq y \leq 0.67$
$Mg_xZn_yCd_{1-x-y}Se$	InP	$y = 0.51 - 0.41x$	$0 \leq x \leq 0.83$

law is exactly valid within the limits of error  $\Delta a/a \leq 4 \times 10^{-4}$  and follows the equation (in Å)

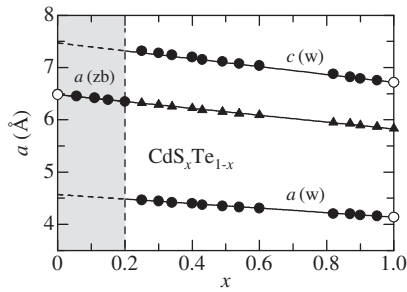
$$a(x) = 6.4822 - 0.3792x \quad (1.16)$$

$CdS_xTe_{1-x}$  shows a zinc-blende–wurtzite crystalline phase change at any alloy composition. Early studies failed to grow alloys for the full range of compositions, concluding that a large

**Figure 1.19** Lattice constant  $a$  as a function of  $x$  for  $Zn_xCd_{1-x}Te$  at 300 K. The experimental data are taken from Schenk *et al.* [32]. The solid line represents the linear best fit of Equation (1.16)

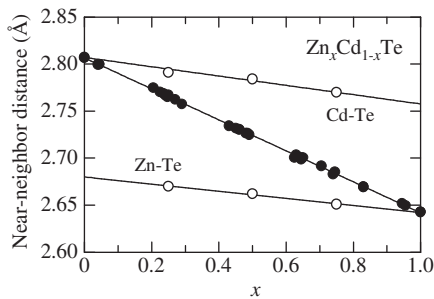
miscibility gap exists in the CdS–CdTe pseudobinary system [33]. In 1973 Ohata *et al.* [34] studied the bulk alloy system for the full range of compositions and reported a change in the crystalline phase at  $x \sim 0.2$ .

Figure 1.20 plots the lattice constants  $a$  and  $c$  versus  $x$  for bulk  $\text{CdS}_x\text{Te}_{1-x}$  crystals as measured by Wood *et al.* [35] using XRD. The composition  $x$  of each pellet was determined independently using PIXE. In Figure 1.20, the phase change occurs at  $x \sim 0.2$ , in agreement with Ohata *et al.* [34]. The solid triangles represent the effective cubic lattice parameters  $a_{\text{eff}} = (\sqrt{3}a^2c)^{1/3}$  defined in Adachi [1]. It can be concluded from Figure 1.20 that the lattice parameters both in the zinc-blende and wurtzite phases obey Vegard law well. It is also understood that if we consider  $a_{\text{eff}}$ , instead of  $a$  or  $c$ , in the wurtzite phase ( $0.2 < x \leq 1.0$ ),  $\text{CdS}_x\text{Te}_{1-x}$  gives the linear relationship between  $a$  and  $x$  over the whole alloy range ( $0 \leq x \leq 1.0$ ).



**Figure 1.20** Lattice constants  $a$  and  $c$  versus  $x$  for bulk  $\text{CdS}_x\text{Te}_{1-x}$  in the zinc-blende (zb) and wurtzite (w) structures at 300 K. The experimental data are taken from Wood *et al.* [35]. The solid triangles represent the effective cubic parameters  $a_{\text{eff}} = (\sqrt{3}a^2c)^{1/3}$

Motta *et al.* [36] carried out EXAFS measurements on  $\text{Zn}_x\text{Cd}_{1-x}\text{Te}$ . These results are shown in Figure 1.21 by the open circles. The solid circles correspond to the XRD data by Schenk *et al.* [32]. We can see that the EXAFS bond lengths in Figure 1.21 change much less than the nearest-neighbor distances determined from the XRD. As in the case of the III–V alloys (Figures 1.16 and 1.17), the XRD lattice parameters in II–VI alloys do not reflect the actual bond lengths of the nearest neighbors. The EXAFS data of Motta *et al.* [36] agreed with a random distribution of atoms in the mixed cation sublattice.



**Figure 1.21** Near-neighbor distance in  $\text{Zn}_x\text{Cd}_{1-x}\text{Te}$  at 300 K. The experimental data (open circles) are taken from Motta *et al.* [36]. The solid circles represent the bond lengths obtained from the XRD data by Schenk *et al.* [32]

## 1.5 COHERENT EPITAXY AND STRAIN PROBLEM

### 1.5.1 Bilayer Model

Recent semiconductor devices usually have multilayer structures. The distribution of strains in multilayer structures is the subject of perennial, great interest since internal strains normally arise in thin epitaxial films during the preparation by heteroepitaxial growth. Internal strains or stresses are a consequence of the mismatch of lattice constants and/or the difference in the thermal expansion coefficients of the individual layers. The strain and stress are related through the fourth-rank elastic stiffness  $[C]$  or compliance tensor  $[S]$  [1].

Let us consider the case of bonding a thin plate of zinc-blende crystal of size  $N_e a_e \times N_e a_e \times t_e$  onto a substrate of a different size  $N_s a_s \times N_s a_s \times t_s$ , where  $N_i$  is the number of lattice atoms along the edge of the crystal plate,  $a_i$  is the lattice constant and  $t_i$  is the thickness of the plate; see Figure 1.22(a) [37]. To achieve a coherent interface,  $N_e$  is set to equal  $N_s$ . Let us assume that  $a_e$  is less than  $a_s$  and thus  $l_e = N_e a_e$  is less than  $l_s = N_s a_s$ . The bonding operation is carried out in the following manner: equal and opposite forces  $F$  are applied to the plates to stretch plate ‘e’ and compress plate ‘s’ uniformly in the lateral direction to the same final dimension  $l_f \times l_f$ . The two plates are then bonded together with a perfect alignment of the atomic planes; see Figure 1.22(b). At the moment when the two plates are bonded together, the composite experiences an applied bending moment given by  $F(t_s + t_e)/2$ , which is counterbalanced by the moment resulting from the internal elastic stress. Finally, the applied forces are relieved, and the moments from the elastic stresses bend the composite in the direction shown in

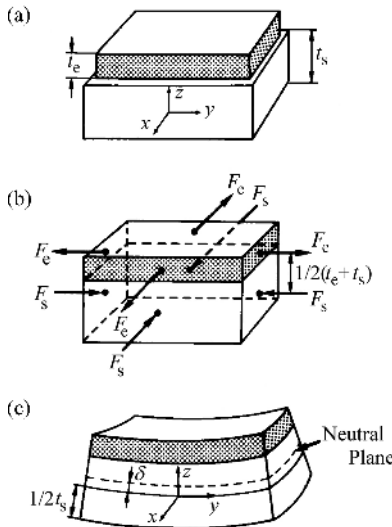


**Figure 1.22** Formation of a two-layer composite: (a) two single-crystalline plates with the lattice constants  $a_e$  and  $a_s$  ( $a_e < a_s$ ) and thicknesses  $t_e$  and  $t_s$ , respectively; (b) layer ‘e’ is stretched and layer ‘s’ is compressed to match the macroscopic dimension, and the two layers are then bonded together to form a composite; (c) the composite bends toward the side with the shorter lattice constant after removal of the external stresses  $F_e$  and  $F_s$

Figure 1.22(c). The bending of the composite relaxes some of the stress, and the radius of curvature is determined by the final state of the internal stress.

Based on this bilayer model, Noyan and Segmüller [37] obtained the coherency condition in terms of the curvature radius  $R$

$$\frac{a_e - a_s}{a_s} = \frac{2}{R} \left[ \frac{t_s}{4} \left( 1 + \frac{a_e t_e}{a_s t_s} \right) + \frac{1}{E_e t_s t_e (1 + t_e/t_s)} \frac{a_e}{a_s} \left( 1 + \frac{a_s E_e t_e}{a_e E_s t_s} \right) \left( \frac{E_s t_s^3}{12} + \frac{E_e t_s^2 t_e}{4} \right) \right] \quad (1.17)$$

where

$$E_i = \frac{Y_i}{1 - P_i} \quad (1.18)$$

with  $Y$  = Young's modulus and  $P$  = Poisson's ratio. The term  $\delta$  shown in Figure 1.22(c) represents the shift of the neutral axis of the composite from  $t_s/2$ . This quantity is given by

$$\delta = \frac{t_e E_e}{2 E_s} \frac{1 + t_e/t_s}{1 + (E_e t_e/E_s t_s)} \quad (1.19)$$

Solving the elastic force and momentum balance equations, Noyan and Segmüller [37] gave the elastic stress component  $X_{xx}$  parallel to the film as

$$X_{xx}^e = - \frac{E_e}{1 + (a_s E_e t_e/a_e E_s t_s)} \frac{a_s}{a_e} \left[ \frac{a_e - a_s}{a_s} - \left( 1 + \frac{a_e t_e}{a_s t_s} \right) \frac{t_s}{2R} \right] \quad (1.20)$$

The relationship between the film and substrate stresses is given by

$$X_{xx}^s = - \frac{t_e}{t_s} X_{xx}^e \quad (1.21)$$

The dependence of  $X_{xx}$  on  $z$  is now given by

$$X_{xx}^e(z) = X_{xx}^e + E_e \left( \frac{z - t_e/2}{R} \right) \quad \text{for } 0 \leq z \leq t_e \quad (1.22a)$$

$$X_{xx}^s(z) = -X_{xx}^e \frac{t_e}{t_s} + E_s \left( \frac{z + t_e/2}{R} \right) \quad \text{for } 0 \geq z \geq -t_s \quad (1.22b)$$

In the case where  $a_e < a_s$ , these expressions give  $X_{xx}^s < 0$ ,  $X_{xx}^e > 0$ , and  $R < 0$ .

## 1.5.2 Elastic Strain and Lattice Deformation

Since  $X_{zz}$  is equal to zero in the bilayer model discussed above, the lattices are free to expand or contract in the  $z$  direction, that is, perpendicular to the interface. As seen in Figure 1.23, this causes the cubic lattice structure to be tetragonally distorted. Since both  $X_{xx}^i$  and  $X_{yy}^i$  have opposite signs for  $i = s$  compared to  $i = e$ , the two cubic lattices are tetragonally distorted in the opposite sense, one with the lattice constant perpendicular to the interface lengthened and

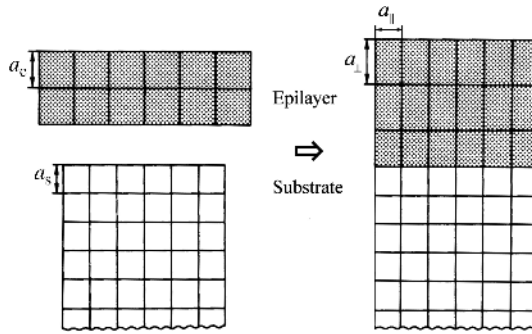


**Figure 1.23** Cross section of an ‘epilayer–substrate’ system, where  $a_e$  and  $a_s$  are the unstrained lattice parameters of the epilayer and substrate, respectively

the other shortened. Therefore, the measured vertical mismatch is enhanced by the tetragonal distortion.

Lattice deformation between the epilayer and substrate can be determined by conventional XRD. For example  $Ga_xIn_{1-x}P_yAs_{1-y}$  epilayers on InP(100) are shown in Figure 1.24 [38], where the  $Ga_xIn_{1-x}P_yAs_{1-y}/InP$  samples were grown by LPE with the Ga atomic fractions in liquid solution between 0.4 and 1.0 at%. The experimental lattice deformation  $\Delta a/a$  perpendicular to the layer surface for layers with a Ga fraction lower than  $\sim 0.0065$  has a positive value (i.e. compressive strain in the growth direction), while it has negative values (tensile strain) for layers with a fraction larger than 0.0065.

In practical cases where the thickness of the epilayer is very small compared to that of the substrate, the lattice mismatch can be taken up totally by the tensile or compressive strain inside the epilayer, giving a coherent interface. A discontinuity in the lattice constant parallel to the interface can exist only in the presence of misfit dislocations. Nagai [39] studied the

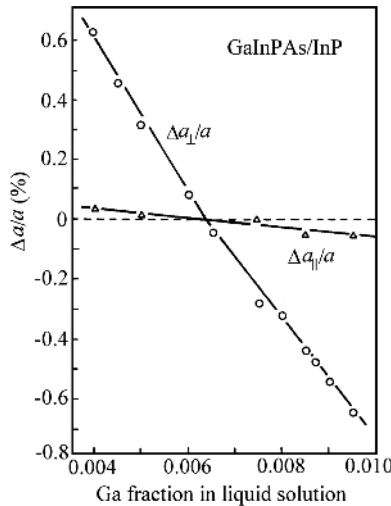


**Figure 1.24** Lattice mismatch in a GaInPAs/InP heterostructure as a function of the Ga atom fraction in LPE-growth liquid solution. [Reprinted with permission from K. Oe and K. Sugiyama, *Appl. Phys. Lett.* **33**, 449 (1978). Copyright (1978) by the American Institute of Physics]

effects of lattice misfit on the lattice deformation for  $\text{Ga}_x\text{In}_{1-x}\text{As}$  on GaAs by HT-VPE. The thickness of the substrates was in the range 2–5 mm and the epilayer was in the range 5–10  $\mu\text{m}$ . His results are shown in Figure 1.25, where  $a_{\parallel}$  is the unstrained lattice parameter of the substrate (GaAs) and  $a_{\perp}$  is the strained lattice parameter of the epilayer due to tetragonal distortion.

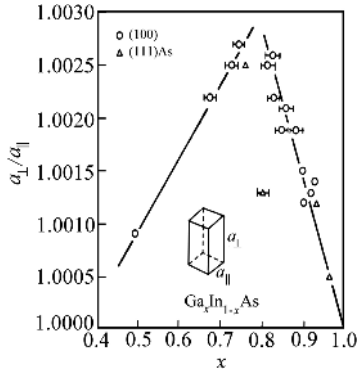


**Figure 1.25** Lattice-constant ratio  $a_{\perp}/a_{\parallel}$  for HT-VPE-grown  $\text{Ga}_x\text{In}_{1-x}\text{As}$  on (1 0 0) and (1 1 1)As planes of GaAs. [Reprinted with permission from H. Nagai, *J. Appl. Phys.* **45**, 3789 (1974). Copyright (1974) by the American Institute of Physics]

The lattice constant of InAs (6.0583 Å) is larger than that of GaAs (5.65330 Å). Thus, the  $\text{Ga}_x\text{In}_{1-x}\text{As}$  lattice on GaAs is expected to be tetragonally distorted with the lattice constant perpendicular to the interface being lengthened. The measured lattice constants perpendicular to the film are indeed larger than that along the surface. In the region  $x > 0.8$  the degree of deformation increased with decreasing  $x$ , but in the region  $x < 0.8$  it decreased with decreasing  $x$ . With the aid of defect revealing etching, it was concluded that in the region  $x > 0.8$  the lattice mismatch is relieved only by tetragonal distortion and for  $x < 0.8$  it is relieved by both misfit dislocation and tetragonal distortion.

Figure 1.26 plots the lattice constant  $a$  versus  $x$  for strained  $\text{C}_x\text{Si}_{1-x}$  alloy grown on Si(100) by solid-source MBE. The experimental data are taken from Berti *et al.* [14]. The dash-dotted

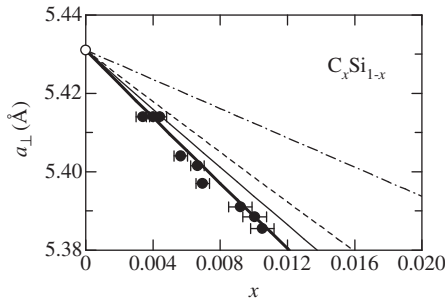


**Figure 1.26** Lattice constant  $a$  versus  $x$  for strained  $\text{C}_x\text{Si}_{1-x}$  grown on Si(1 0 0) by solid-source MBE. The experimental data are taken from Berti *et al.* [14]. The dash-dotted line represents the linearly interpolated values between diamond and Si. The light solid and dashed lines are calculated from Equation (1.23) by introducing  $a_0$  values estimated from Vegard law between Si and 3C-SiC ( $x = 0.5$ ) and between Si and C ( $x = 1.0$ ), respectively. The heavy solid line is calculated by introducing the Monte Carlo-simulated lattice constants reported by Kelires [13] as  $a_0$

line shows the linear interpolation result between diamond ( $a = 3.5670 \text{ \AA}$ ) and Si ( $a = 5.4310 \text{ \AA}$ ). We can see that the linear interpolation scheme predicts quite different lattice parameters from the experimental data.

The strain in the epilayer and hence the lattice constant in growth direction  $a_{\perp}$  can be calculated from the elastic theory [37]

$$a_{\perp} = (a_0 - a_{\parallel}) \left( 1 + \frac{2P}{1-P} \right) + a_{\parallel} \quad (1.23)$$

where  $a_0$  is the lattice constant of the relaxed material,  $a_{\parallel}$  is the in-plane lattice constant assumed to be the same as the substrate parameter and  $P$  is Poisson's ratio. In the case of cubic materials, Equation (1.23) can be rewritten as

$$a_{\perp} = (a_0 - a_{\parallel}) \left( 1 + \frac{2C_{12}}{C_{11}} \right) + a_{\parallel} \quad (1.24)$$

where  $C_{ij}$  is the elastic stiffness constant.

The light solid and dashed lines in Figure 1.26 represent the calculated results of Equation (1.23) by introducing  $a_0$  values estimated from Vegard law between Si and 3C-SiC ( $x = 0.5$ ) and between Si and diamond ( $x = 1.0$ ), respectively (Figure 1.6). The heavy solid line is also obtained from Equation (1.23) by introducing Monte Carlo-simulated lattice constants [13] as  $a_0$ . The  $P$  values in Equation (1.23) are obtained from the linear interpolation between diamond and Si [1]. The results in Figure 1.26 suggest that the lattice constant  $a$  in  $C_xSi_{1-x}$  significantly deviates from Vegard law. The relationship between  $a$  and  $x$  can be finally given by Equation (1.3).

Figure 1.27 shows the lattice parameters perpendicular and parallel to the epilayer surface of MOMBE-grown  $GaN_xAs_{1-x}$  on GaAs(100) [40]. The experimental data clearly suggest that the  $GaN_xAs_{1-x}$  layers are coherently grown on the GaAs(100) substrates. The dashed line is simply estimated from the linear interpolation between  $c$ -GaN and GaAs. The solid lines are calculated from Equation (1.23) with  $a_{\parallel} = 5.6517 \text{ \AA}$ . The relaxed parameter  $a_0$  and Poisson's ratios used in the calculation are taken from Vegard law between  $c$ -GaN and GaAs [1]. We can see in Figure 1.27 excellent agreement between the calculated and experimental lattice parameters.

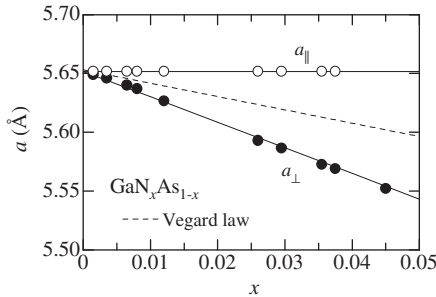


**Figure 1.27** Lattice parameters perpendicular ( $a_{\perp}$ ) and parallel ( $a_{\parallel}$ ) to the epilayer surface of MOMBE-grown dilute-nitride  $GaN_xAs_{1-x}$  on GaAs(100). The experimental data are taken from Uesugi *et al.* [40]. The dashed line is simply estimated from Vegard law between  $c$ -GaN and GaAs. The solid lines are calculated from Equation (1.23) with  $a_{\parallel} = 5.6517 \text{ \AA}$  (const.). The relaxed parameters  $a_0$  and Poisson's ratios  $P$  are taken from Vegard law between  $c$ -GaN and GaAs

The essentially same analysis as in Figure 1.27 is performed on strained  $\text{Al}_x\text{Ga}_{0.9-x}\text{In}_{0.1}\text{N}$  grown by MOCVD [24]. The solid line in Figure 1.14 represents the result of this analysis. Note that Poisson's ratio is a crystallographic plane- and direction-dependent quantity. The expressions of Poisson's ratio  $P$  and corresponding numeric values for some hexagonal semiconductors are summarized in Tables 3.19 and 3.20 of Adachi [1]. The quaternary  $P$  values used in Equation (1.23) are estimated from Vegard law. The in-plane lattice constant  $a_{\parallel}$  is assumed to be 5.240 Å. In Figure 1.14, there is good agreement between the calculated and experimental values even in the wurtzite crystal structure. However, in the case of relaxed  $\text{Al}_x\text{In}_{1-x}\text{N}$  alloy Vegard law leads to an overestimation of the In mole fraction, which cannot be explained by either strain state or impurity levels. The In atomic fraction can be overestimated by as much as 6–37% in the range of  $0.18 < x < 0.93$  [41].

Figures 1.28(a) and 1.28(b) show the experimental lattice parameters  $a$  and  $c$  for  $\text{Mg}_x\text{Zn}_{1-x}\text{O}$  layers on sapphire (0001) [42] and on 6H-SiC (0001) [43]. The solid lines show the linear interpolation results of  $c$  and  $a$  between MgO and ZnO. The effective cubic lattice parameters  $a_{\text{eff}} = (\sqrt{3}a^2c)^{1/3}$  for MgO and ZnO are, respectively, 4.484 and 4.567 Å, while those for sapphire and 6H-SiC are 6.335 Å and 4.359 Å, respectively. Coherently grown  $\text{Mg}_x\text{Zn}_{1-x}\text{O}$  films on the sapphire and 6H-SiC substrates will be tensile- and compressive-strained, respectively. The ZnO ( $x=0$ ) layers, however, exhibited virtually relaxed lattice constants of 3.246 and 5.205 Å along the  $a$  and  $c$  axes, respectively. As seen in Figure 1.28, the  $c$ - ( $a$ -) axis length decreased (increased) with increasing  $x$  for  $\text{Mg}_x\text{Zn}_{1-x}\text{O}$  both on the sapphire and 6H-SiC substrates. The resulting ratio  $c/a$  decreased with increasing  $x$ , indicating that the  $\text{Mg}_x\text{Zn}_{1-x}\text{O}$  films are considerably distorted from the ideal wurtzite although they are in the relaxed states.

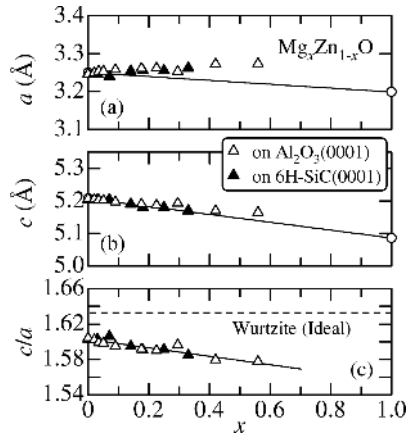


**Figure 1.28** (a)  $a$ -axis and (b)  $c$ -axis lattice parameters at 300 K for  $\text{Mg}_x\text{Zn}_{1-x}\text{O}$  grown on  $\text{Al}_2\text{O}_3$  (0001) substrate by Ohtomo *et al.* [42] and on 6H-SiC (0001) substrate by Ashrafi and Segawa [43]. The solid lines in (a) and (b) show the linearly interpolated values of  $a$  and  $c$  between MgO and ZnO. The corresponding  $c/a$  ratios are plotted in (c)

### 1.5.3 Critical Thickness

Pseudomorphic epitaxy, in which a high-quality thin film is epitaxially grown on a lattice-mismatched substrate, has found its application in many areas [44]. SLs and QWs are high-quality multilayered structures grown from lattice matched and mismatched materials.

The large lattice mismatch is totally accommodated by uniform elastic strains in the layers if the layer thicknesses are kept below certain critical values. The idea for thin films emerged from a critical layer thickness  $h_c$  below which a dislocation-free, coherently strained interface would be stable and above which a misfit dislocation structure and semi-coherent interface would be stable. Knowledge of the so-called critical thickness is essential for realizing the advantages of lattice-mismatched heterostructure systems.

The critical thickness  $h_c$  of an epilayer, which was first considered by Frank and van der Merwe [45], is a parameter introduced to explain the experimental observation of coherent, pseudomorphic or strained-layer epitaxy. The breakdown of coherency can be determined in several ways. XRD and PL are commonly employed methods of determining the loss of coherency by demonstrating a change in average lattice constant (XRD) or a shift in PL peak energy and a reduction in PL intensity, following the release of strain. TEM is the direct manifestation of the breakdown of coherency.

We show in Figure 1.29 the critical thickness  $h_c$  versus  $x$  for (a)  $\text{Si}_x\text{Ge}_{1-x}$  layer on Si, (b)  $\text{Ga}_x\text{In}_{1-x}\text{As}$  layer on InP and (c)  $\text{GaN}_x\text{As}_{1-x}$  layer on GaAs, respectively. Note that  $x = 0.47$  in Figure 1.29(b) is the lattice-matching composition to InP.

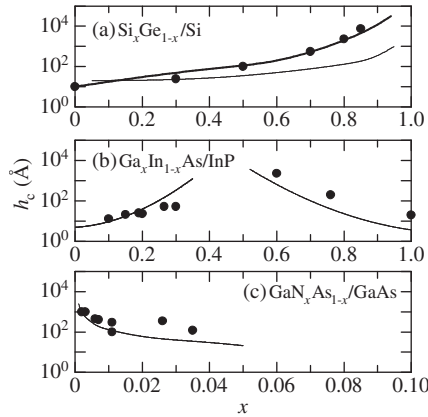


**Figure 1.29** Critical thickness  $h_c$  versus  $x$  for (a)  $\text{Si}_x\text{Ge}_{1-x}$  layer on Si, (b)  $\text{Ga}_x\text{In}_{1-x}\text{As}$  layer on InP and (c)  $\text{GaN}_x\text{As}_{1-x}$  layer on GaAs. The solid lines represent the theoretical model of Matthews and Blakeslee [46]. The heavy solid line in (a) is obtained from an energy-balanced misfit dislocation generation model by People and Bean [47]

Although several theories have been proposed to predict  $h_c$  [44], most semiconductor device designers rely upon the model of Matthews and Blakeslee [46]. The solid lines in Figure 1.29 show the results based on this model. The experimental  $h_c$  data usually exceed the Matthews–Blakeslee’s prediction. It is also understood that for  $\text{Si}_x\text{Ge}_{1-x}$  there is little dependence of  $h_c$  on  $x$ . The heavy solid line in Figure 1.29(a) represents the theoretical curve obtained from an energy-balanced misfit dislocation generation model by People and Bean [47]. This model is in excellent agreement with the experimental data.

The critical thicknesses  $h_c$  for  $\text{Al}_x\text{Ga}_{1-x}\text{N}$  and  $\text{Ga}_x\text{In}_{1-x}\text{N}$  on relaxed GaN layers were measured by Akasaki and Amano [48]. The experimental  $h_c$  values were in the range 300 to 700 nm for  $\text{Al}_x\text{Ga}_{1-x}\text{N}/\text{GaN}$  ( $0.05 \leq x \leq 0.2$ ) and  $\sim 40$  nm for  $\text{Ga}_x\text{In}_{1-x}\text{N}/\text{GaN}$  ( $0.8 \leq x \leq 0.95$ ).

The  $h_c$  values for  $\text{Si}_x\text{Ge}_{1-x}/\text{Si}$  and some III–V and II–VI semiconductors grown on various lattice-mismatched substrates are summarized in Figure 1.30. The solid lines are obtained by least-squares fitting with ( $h_c$  in Å,  $\Delta a/a$  in at%)

$$h_c = \left( \frac{A}{\Delta a/a} \right)^n \quad (1.25)$$

with  $A = 7.5$  and  $n = 3.5$  for  $\text{Si}_x\text{Ge}_{1-x}/\text{Si}$ ,  $A = 16$  and  $n = 2.4$  for III–V semiconductors and  $A = 52$  and  $n = 1.5$  for II–VI semiconductors. It should be noted that the II–VI semiconductors have weak bond strength. The dislocation energy in such semiconductors is much smaller than those in  $\text{Si}_x\text{Ge}_{1-x}/\text{Si}$  and III–V semiconductors. Therefore, dislocations can be more easily generated in the II–VI semiconductors.

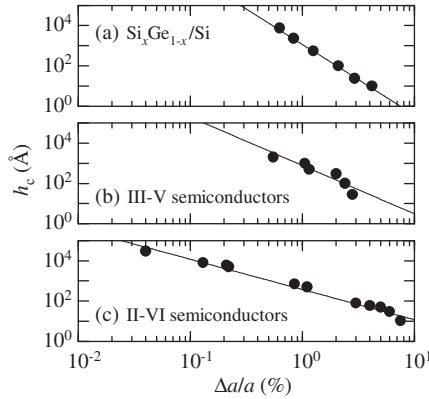


**Figure 1.30** Critical thickness  $h_c$  for (a)  $\text{Si}_x\text{Ge}_{1-x}$ , (b) III–V and (c) II–VI semiconductors grown on various lattice-mismatched substrates. The solid lines represent the least-squares fit using Equation (1.25)

## 1.6 STRUCTURAL PHASE TRANSITION

At high pressure the group-IV elemental semiconductors show metallic transitions in a sequence from cubic (diamond)  $\rightarrow$  tetragonal ( $\beta$ -Sn)  $\rightarrow$  simple hexagonal  $\rightarrow$  hexagonal close packed. Similarly, the III–V and II–VI binary semiconductors exhibit a variety of the crystal structures at high pressures. In Tables 1.8 and 1.9 of Adachi [1], transition pressure to the first phase ( $P_T$ ) and transition sequences can be found for some group-IV, III–V and II–VI semiconductors. The additional data are:  $P_T = 56$  GPa (zinc-blende  $\rightarrow$  hexagonal (NiAs)) for BeSe;  $P_T = 35$  GPa (zincblende  $\rightarrow$  hexagonal (NiAs)) for BeTe; and  $P_T = 90.6$  GPa (rocksalt  $\rightarrow$  CsCl) for CdO.

There are a very few studies on the structural phase transition in semiconductor alloys. Some of these studies are summarized in Table 1.16. Webb *et al.* [49] observed the phase transition in  $\text{Zn}_x\text{Cd}_{1-x}\text{Te}$  from the zinc-blende to rocksalt structures. However, the recent studies on ZnTe and CdTe suggest the presence of cinnabar phase between the zinc-blende and rocksalt structures [50]. Vnuk *et al.* [51] studied the effect of pressure on semiconductor

**Table 1.16** Phase-transition sequence observed for some III–V and II–VI ternaries at high pressures. zb = zinc-blende; or = orthorhombic; w = wurtzite; rs = rocksalt (NaCl); cin = cinnabar

System	Material	Sequence	Ref.
III–V	$\text{Ga}_x\text{In}_{1-x}\text{P}$	semiconductor $\rightarrow$ metal (optical absorption)	<i>a</i>
	$\text{Al}_x\text{Ga}_{1-x}\text{As}$	zb $\rightarrow$ or ( <i>Pmm2</i> )/or ( <i>Cmcm</i> ) (GaAs like)	<i>b</i>
	$\text{Ga}_x\text{In}_{1-x}\text{Sb}$	zb $\rightarrow$ $\beta$ -Sn	<i>c</i>
II–VI	$\text{Mg}_x\text{Zn}_{1-x}\text{O}$	w $\rightarrow$ rs	<i>d</i>
	$\text{Zn}_x\text{Cd}_{1-x}\text{S}$	zb $\rightarrow$ rs	<i>e</i>
	$\text{Zn}_x\text{Cd}_{1-x}\text{Se}$	zb $\rightarrow$ rs ( $x=0.9$ )	<i>f</i>
		semiconductor $\rightarrow$ metal ( $0 \leq x \leq 0.32$ )	<i>g</i>
	$\text{Zn}_x\text{Cd}_{1-x}\text{Te}$	zb $\rightarrow$ rs	<i>h</i>
	$\text{ZnS}_x\text{Se}_{1-x}$	semiconductor $\rightarrow$ metal (resistance)	<i>i</i>
	$\text{ZnSe}_x\text{Te}_{1-x}$	zb $\rightarrow$ cin $\rightarrow$ rs ( $0 \leq x \leq 0.55$ )	<i>j</i>
		zb $\rightarrow$ rs ( $0.55 < x \leq 1$ )	<i>j</i>

- <sup>a</sup>A. R. Goñi *et al.*, *Phys. Rev. B* **39**, 3178 (1989)
- <sup>b</sup>W. Paszkowicz *et al.*, *Acta Phys. Pol. A*, **91**, 993 (1997)
- <sup>c</sup>C. Y. Liu *et al.*, *J. Phys. Chem. Solids* **39**, 113 (1978)
- <sup>d</sup>J. A. Sans and A. Segura, *High Pressure Res.* **24**, 119 (2004)
- <sup>e</sup>A. Béliveau and C. Carlone, *Phys. Rev. B* **44**, 3650 (1991)
- <sup>f</sup>C.-M. Lin *et al.*, *Phys. Rev. B* **58**, 16 (1998)
- <sup>g</sup>Y. C. Lin *et al.*, *J. Appl. Phys.* **101**, 073507 (2007)
- <sup>h</sup>A. W. Webb *et al.*, *J. Appl. Phys.* **61**, 2492 (1987)
- <sup>i</sup>S. R. Tiong *et al.*, *Jpn. J. Appl. Phys.* **28**, 291 (1989)
- <sup>j</sup>J. Pellicer-Porres *et al.*, *Phys. Rev. B* **71**, 035210 (2005)

( $\alpha$ -Sn)-to-metal ( $\beta$ -Sn) transition temperature in dilute  $\text{Ge}_x\text{Sn}_{1-x}$  ( $x \leq 1$  at%). They obtained a slope of  $-48.4 \pm 6$  K/kbar, in good agreement with thermodynamic prediction.

Figure 1.31 plots the transition pressure to the first phase  $P_T$  versus  $x$  for  $\text{Ga}_x\text{In}_{1-x}\text{Sb}$ . The experimental data are taken from Liu *et al.* [52]. A slight bowing can be found in the  $P_T$  versus

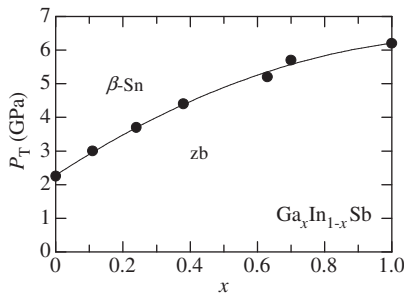


**Figure 1.31** Transition pressure to the first phase  $P_T$  versus  $x$  for  $\text{Ga}_x\text{In}_{1-x}\text{Sb}$ . The experimental data are taken from Liu *et al.* [52]. The solid line shows the quadratic-fit result using Equation (1.26). zb = zinc-blende

$x$  plots. The solid line shows the best-fit result of the quadratic expression (in GPa)

$$P_T(x) = 2.3 + 6.5x - 2.6x^2 \tag{1.26}$$

The transition pressures to the first phase  $P_T$  against alloy composition  $x$  for some II–VI semiconductors are shown in Figure 1.32. The experimental data are taken for  $Zn_xCd_{1-x}S$  from Béliveau and Carlone [53], for  $ZnS_xSe_{1-x}$  from Tiong *et al.* [54] and for  $ZnSe_xTe_{1-x}$  from Pellicer-Porres *et al.* [55]. In Figure 1.32(c), the transition pressure to the second phase is also plotted with the open circles. The linear interpolation is concluded to be an efficient tool to estimate the phase transition pressure in semiconductor alloys.

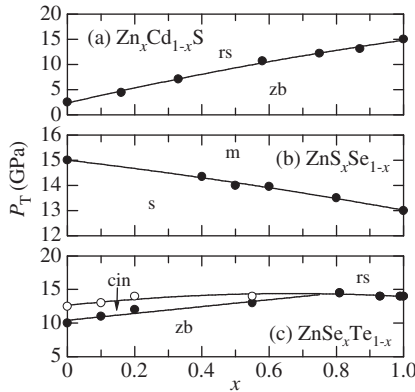


**Figure 1.32** Transition pressures to the first phase  $P_T$  against  $x$  for (a)  $Zn_xCd_{1-x}S$ , (b)  $ZnS_xSe_{1-x}$  and (c)  $ZnSe_xTe_{1-x}$ . The transition pressure to the second phase is plotted in (c) by the open circles. The experimental data are taken for (a)  $Zn_xCd_{1-x}S$  from Béliveau and Carlone [53], for (b)  $ZnS_xSe_{1-x}$  from Tiong *et al.* [54] and for (c)  $ZnSe_xTe_{1-x}$  from Pellicer-Porres *et al.* [55]. cin = cinnabar; m = metal; rs = rocksalt (NaCl); s = semiconductor; zb = zinc-blende

## 1.7 CLEAVAGE PLANE

### 1.7.1 Cleavage

The cleavage properties of a crystal are strongly related to the atomic arrangement and corresponding electron density map. The most readily cleaved crystallographic planes can then be determined only by the crystalline structure. They are (111) plane for alloys of diamond type, (1 1 0) plane for zinc-blende type, (11 $\bar{2}$ 0) and (10 $\bar{1}$ 0) planes for wurtzite type and (100) plane for rocksalt type [1].

### 1.7.2 Surface Energy

The cleavage energy is assumed equal to twice the surface energy of that plane. There is a dearth of experimental measurements on surface energy. The surface energies for several group-VI elemental, III–V and II–VI binary semiconductors are listed in Tables 1.11–1.13 of Adachi [1]. No surface energy data are available for semiconductor alloys.

## REFERENCES

- [1] S. Adachi, *Properties of Group-IV, III-V and II-VI Semiconductors*, John Wiley & Sons Ltd, Chichester, 2005.
- [2] A. Mascarenhas, *Spontaneous Ordering in Semiconductor Alloys*, Kluwer Academic, New York, 2002.
- [3] A. Ourmazd and J. C. Bean, *Phys. Rev. Lett.* **55**, 765 (1985).
- [4] J. Schilz and V. N. Romanenko, *J. Mater. Sci.: Mater. Electron.* **6**, 265 (1995).
- [5] T. S. Kuan, T. F. Kuech, W. I. Wang, and E. L. Wilkie, *Phys. Rev. Lett.* **54**, 201 (1985).
- [6] T. Suzuki, in A. Mascarenhas, *Spontaneous Ordering in Semiconductor Alloys*, Kluwer Academic, New York, 2002, p. 1.
- [7] A. Gomyo, M. Sumino, I. Hino, and T. Suzuki, *Jpn. J. Appl. Phys.* **34**, L469 (1995).
- [8] A. Gomyo, K. Makita, I. Hino, and T. Suzuki, *Phys. Rev. Lett.* **72**, 673 (1994).
- [9] A. A. Mbaye, L. G. Ferreira, and A. Zunger, *Phys. Rev. Lett.* **58**, 49 (1987).
- [10] H. S. Lee, S. Yi, T. W. Kim, Y. J. Park, J. Y. Lee, M. S. Kwon, and H. L. Park, *Solid State Commun.* **137**, 70 (2006).
- [11] R. A. Soref, *Proc. IEEE* **81**, 1687 (1993).
- [12] E. T. Croke, A. T. Hunter, C. C. Ahn, T. Laursen, D. Chandrasekhar, A. E. Bair, D. J. Smith, and J. W. Mayer, *J. Cryst. Growth* **175-176**, 486 (1997).
- [13] P. C. Kelires, *Phys. Rev. B* **55**, 8784 (1997).
- [14] M. Berti, D. D. Salvador, A. V. Drigo, F. Romanato, J. Stangl, S. Zerlauth, F. Schäffler, and G. Bauer, *Appl. Phys. Lett.* **72**, 1602 (1998).
- [15] J. P. Dismukes, L. Ekstrom, and R. J. Paff, *J. Phys. Chem.* **68**, 3021 (1964).
- [16] M. Matsuura, J. M. Tonnerre, and G. S. Cargill III, *Phys. Rev. B* **44**, 3842 (1991).
- [17] H. Kajiyama, S. Muramatsu, T. Shimada, and Y. Nishino, *Phys. Rev. B* **45**, 14005 (1992).
- [18] I. Yonenaga, M. Sakurai, M. H. F. Sluiter, Y. Kawazoe, and S. Muto, *J. Mater. Sci.: Mater. Electron.* **16**, 429 (2005).
- [19] N. S. Takahashi, in *Properties of Aluminium Gallium Arsenide*, EMIS Datareviews Series No. 7 (edited by S. Adachi), INSPEC, London, 1993, p. 3.
- [20] R. E. Nahory, M. A. Pollack, W. D. Johnston, Jr., and R. L. Barns, *Appl. Phys. Lett.* **33**, 659 (1978).
- [21] F. Germini, C. Bocchi, C. Ferrari, S. Franchi, A. Baraldi, R. Magnanini, D. D. Salvador, M. Berti, and A. V. Drigo, *J. Phys. D: Appl. Phys.* **32**, A12 (1999).
- [22] J. D. Bearch, H. Al-Thani, S. McCray, R. T. Collins, and J. A. Turner, *J. Appl. Phys.* **91**, 5190 (2002).
- [23] L. T. Romano, B. S. Krusor, M. D. McCluskey, and D. P. Bour, *Appl. Phys. Lett.* **73**, 1757 (1998).
- [24] M. E. Aumer, S. F. LeBoeuf, F. G. McIntosh, and S. M. Bedair, *Appl. Phys. Lett.* **75**, 3315 (1999).
- [25] G. Bisognin, D. D. Salvador, C. Mattevi, M. Berti, A. V. Drigo, G. Ciatto, L. Grenouillet, P. Duvaut, G. Gilet, and H. Mariette, *J. Appl. Phys.* **95**, 48 (2004).
- [26] S. Z. Wang, S. F. Yoon, W. J. Fan, W. K. Loke, T. K. Ng, and S. Z. Wang, *J. Appl. Phys.* **96**, 2010 (2004).
- [27] G. Fournet, *J. Phys. Radium* **14**, 374 (1953).
- [28] J. C. Mikkelsen, Jr., and J. B. Boyce, *Phys. Rev. Lett.* **49**, 1412 (1982); *Phys. Rev. B* **28**, 7130 (1983)
- [29] H. Oyanagi, Y. Takeda, T. Matsushita, T. Ishiguro, and A. Sasaki, in *Gallium Arsenide and Related Compounds*, IOP, Bristol, 1986, p. 295.
- [30] N. J. Jeffe, A. V. Blant, T. S. Cheng, C. T. Foxon, C. Bailey, P. G. Harrison, J. F. W. Mosselmans, and A. J. Dent, *Mater. Res. Soc. Symp. Proc.* **512**, 519 (1998).
- [31] T. Mattila and A. Zunger, *J. Appl. Phys.* **85**, 160 (1999).
- [32] M. Schenk, I. Hähnert, L. T. H. Duong, and H.-H. Niebsch, *Cryst. Res. Technol.* **31**, 665 (1996).
- [33] E. Cruceanu and D. Niculesciu, *Compt. Rend. Acad. Sci.* **261**, 935 (1965).
- [34] K. Ohata, J. Saraale, and T. Tanaka, *Jpn. J. Appl. Phys.* **12**, 1198 (1973).
- [35] D. A. Wood, K. D. Rogers, D. W. Lane, G. J. Conibeer, and D. Parton, *J. Mater. Sci. Lett.* **17**, 1511 (1998).

- [36] N. Motta, A. Balzarotti, P. Letardi, A. Kisiel, M. T. Czyzyk, M. Zimnal-Starnawska, and M. Podgorny, *Solid State Commun.* **53**, 509 (1985).
- [37] I. C. Noyan and A. Segmüller, *J. Appl. Phys.* **60**, 2980 (1986).
- [38] K. Oe and K. Sugiyama, *Appl. Phys. Lett.* **33**, 449 (1978).
- [39] H. Nagai, *J. Appl. Phys.* **45**, 3789 (1974).
- [40] K. Uesugi, N. Morooka, and I. Suemune, *Appl. Phys. Lett.* **74**, 1254 (1999).
- [41] T. Seppänen, L. Hulman, J. Birch, M. Beckers, and U. Kreissig, *J. Appl. Phys.* **101**, 043519 (2007).
- [42] A. Ohtomo, M. Kawasaki, T. Koida, K. Masubuchi, H. Koinuma, Y. Sakurai, Y. Yoshida, T. Yasuda, and Y. Segawa, *Appl. Phys. Lett.* **72**, 2466 (1998).
- [43] A. B. M. A. Ashrafi and Y. Segawa, *J. Vac. Sci. Technol. B* **23**, 2030 (2005).
- [44] S. Jain, M. Willander, and R. Van Overstraeten, *Compound Semiconductors Strained Layers and Devices*. Kluwer Academic, Boston, 2000.
- [45] F. C. Frank and J. H. van der Merwe, *Proc. Roy. Soc. A* **201**, 261 (1950).
- [46] J. W. Matthews and A. E. Blakeslee, *J. Cryst. Growth* **27**, 118 (1974).
- [47] R. People and J. C. Bean, *Appl. Phys. Lett.* **49**, 229 (1986).
- [48] I. Akasaki and H. Amano, in *Semiconductors and Semimetals*, Vol. **50** (edited by J. I. Pankove and T. D. Moustakas), Academic, New York, 1998, p. 459.
- [49] A. W. Webb, S. B. Qadri, E. R. Carpenter, Jr., E. F. Skelton, and J. Kennedy, *J. Appl. Phys.* **61**, 2492 (1987).
- [50] S. Adachi, *Handbook on Physical Properties of Semiconductors: Volume 3 II–VI Semiconductors*. Kluwer Academic, Boston, 2004.
- [51] F. Vnuk, A. D. Monte, and R. W. Smith, *J. Appl. Phys.* **55**, 4171 (1984).
- [52] C. Y. Liu, I. L. Spain, and E. F. Skelton, *J. Phys. Chem. Solids* **39**, 113 (1978).
- [53] A. Béliveau and C. Carlone, *Phys. Rev. B* **44**, 3650 (1991).
- [54] S. R. Tiong, M. Hiramatsu, Y. Matsushima, and E. Ito, *Jpn. J. Appl. Phys.* **28**, 291 (1989).
- [55] J. Pellicer-Porres, D. Martínez-García, Ch. Ferrer-Roca, A. Segura, and V. Muñoz-Sanjosé, *Phys. Rev. B* **71**, 035210 (2005).

